Aircraft Observations of Cumulus Microphysics Ranging from the Tropics to Midlatitudes: Implications for a "New" Secondary Ice Process

PAUL LAWSON, COLIN GURGANUS, AND SARAH WOODS

SPEC Incorporated, Boulder, Colorado

ROELOF BRUINTJES

National Center for Atmospheric Research,[a] *Boulder, Colorado*

(Manuscript received 8 February 2017, in final form 7 June 2017)

ABSTRACT

In situ data collected by three research aircraft in four geographical locations are analyzed to determine the relationship between cloud-base temperature, drop size distribution, and the development of supercooled water drops and ice in strong updraft cores of convective clouds. Data were collected in towering cumulus and feeder cells in the Caribbean, over the Gulf of Mexico, over land near the Gulf Coast, over land in the southeastern United States, and the high plains in Colorado and Wyoming. Convective clouds in the Caribbean, over the Gulf of Mexico and its coast, and over the southeastern United States all develop millimeter-diameter supercooled drops in updraft cores. Clouds over the high plains do not generate supercooled large drops, and rarely are drops $>70\,\mu$m observed in updraft cores. Commensurate with the production of supercooled large drops, ice is generated and rapidly glaciates updraft cores through a hypothesized secondary ice process that is based on laboratory observations of large drops freezing and emitting tiny ice particles. Clouds over the high plains do not experience the secondary ice process and significant concentrations of supercooled liquid in the form of small drops are carried much higher (up to $-35.5°$C) in the updraft cores. An empirical relationship that estimates the maximum level to which supercooled liquid water will be transported, based on cloud-base drop size distribution and temperature, is developed. Implications have applications for modeling the transport of water vapor and particles into the upper troposphere and hygroscopic seeding of cumulus clouds.

1. Introduction

Microphysical observations have shown that the rate of glaciation of updraft cores differs markedly in tropical maritime cumulus clouds when compared with the glaciation of updraft cores in midlatitude continental cumuli. Koenig (1963) observed that high concentrations of ice and graupel were observed within 5–10 min after millimeter-diameter supercooled drops formed in tropical cumulus clouds with tops warmer than $-10°$C. Lawson et al. (2015, hereafter L15) documented the rapid glaciation of updraft cores in maritime clouds using a Learjet that climbed with the ascending updrafts and collected data with state-of-the-art instrumentation. The authors hypothesize that a secondary ice process (SIP) was active based on laboratory work showing that large (80–400-μm diameter) supercooled drops emitted small fragments upon freezing (Leisner et al. 2014; Lauber et al. 2016; Wildeman et al. 2017). In contrast to tropical maritime clouds, measurements in midlatitude continental clouds show that updraft cores do not develop large ($>\sim70\,\mu$m) supercooled drops (Cannon et al. 1974; Heymsfield et al. 1979; Dye et al. 1974, 1986; and measurements presented in this study). Heymsfield et al. (1979) report that undiluted updraft cores with small supercooled drops exist up to $-18°$C in midlatitude cumuli, and possibly colder, but there were inadequate sailplane data at colder temperatures. Rosenfeld and Woodley (2000) report up to $1.8\,\mathrm{g\,m^{-3}}$ liquid water with a mean drop diameter of $17\,\mu$m at a temperature of $-37.5°$C in vigorous cumulus over west Texas. Later in this paper, we show measurements of supercooled liquid water at $-35.5°$C using the cloud particle imager (CPI),

[a] The National Center for Atmospheric Research is sponsored by the National Science Foundation.

Corresponding author: Dr. Paul Lawson, plawson@specinc.com

DOI: 10.1175/JAS-D-17-0033.1

which has been shown to distinguish spherical (water drops) from nonspherical (ice particles) based on images $>\sim 30\,\mu$m in diameter (L15).

Convective cloud microphysics have a strong influence on global hydrology and the earth radiative budget. The percentage of condensate that rains out, evaporates, or is transported into the anvil is a strong function of microphysics (Grabowski and Morrison 2016). Liu and Curry (1999) analyzed satellite data over the tropics and found that ice water path has a strong correlation with rainfall rate. Connolly et al. (2006) have shown that the maximum vertical velocity, the cloud-top height, and the anvil ice water content of a deep convective storm were sensitive to enhanced SIP rates leading to a net radiative forcing of $10\,\mathrm{W\,m^{-2}}$. Data from the Cloud–Aerosol Lidar with Orthogonal Polarization (CALIOP) satellite-based lidar suggest that there is more ice above 15 km over land than over oceans in the upper troposphere–lower stratosphere (UTLS), implying that continental convection tends to transport more ice into the UTLS (Avery et al. 2015). This has implications for climate modeling, where characteristics of the anvil affect the atmospheric radiative balance (e.g., Lawson et al. 2010), and cloud-top height is important for water distribution in the troposphere and transfer into the stratosphere (Hardiman et al. 2015). It is well established that increased water vapor in the stratosphere has a large impact on warming of the troposphere (Forster and Shine 2002; Solomon et al. 2010).

In this paper, we report results from aircraft in situ measurements of the microphysics and dynamics of updraft cores in maritime tropical convective clouds (Caribbean); maritime extratropical convective clouds (Gulf of Mexico); continental convection with warm, low-altitude cloud bases [southeastern United States (SEUS)]; and midlatitude continental convective clouds with cold, high-altitude cloud bases (the high plains of Colorado and Wyoming). We find that the cloud microphysical properties exhibit a monotonic trend from the Caribbean to the midlatitudes. Basically, the lower and warmer the cloud base, and the broader the cloud-base drop size distribution (DSD), the greater the probability of developing supercooled large drops (drizzle and rain) in the updraft cores. We further postulate that the development of supercooled large drops (SLDs)[1] is strongly correlated with rapid glaciation via the hypothesized SIP. We develop an empirical relationship between the temperature at which rapid glaciation occurs as a function of the product of cloud-base DSD and temperature. This relationship may be used as a check on numerical simulations of strong updraft cores in cumulus clouds.

[1] We use the term supercooled large drop here (which is typically employed in icing studies) because it is defined by the World Meteorological Organization as a supercooled drop with a diameter $>$ $50\,\mu$m, and this definition is consistent with its usage in this study.

2. Meteorology

Toon et al. (2016) provide a detailed description of the meteorology associated with the National Aeronautics and Space Administration (NASA) Studies of Emissions, Atmospheric Composition, Clouds and Climate Coupling by Regional Surveys (SEAC^{4}RS) project. SEAC^{4}RS meteorology was complex and varied from the initial stage of the project (6–21 August 2013) to the second stage of the project (22 August–23 September). According to Toon et al. (2016), SEAC^{4}RS took place during a transition period from a summer regime when there are strong quasi-stationary large-scale troughs and ridges, to a fall regime with traveling waves. The initial stage was dominated by isolated convection, while the latter stage saw more mesoscale and synoptic convection. Rainfall, a proxy for convection, is shown in Fig. 1 for two periods during SEAC^{4}RS. The convective clouds and cloud systems studied during SEAC^{4}RS ranged from small isolated cumulus congestus to deep, organized convective systems with strong outflow that formed anvils and occasional overshooting tops. The following general description is adapted from Toon et al. (2016, p. 4979): "During SEAC^{4}RS there were many occasions when small cumulus [congestus] were present at the top of the boundary layer over the SEUS. SEAC^{4}RS also sampled many deep convective systems in a variety of aerosol environments over land and over the Gulf of Mexico."

It is important to note that this paper does not include measurements from organized mesoscale systems, such as squall lines, supercells, and mesoscale convective complexes that all have lifetimes on the order of 6–12 h. Both the Learjet and DC-8 relied on onboard weather radar as well as satellite and radar products uploaded from the ground to help identify regions that would be unsafe for flight. Thus, measurements from cloud penetrations are limited to regions in mixed-phase clouds where graupel particles did not exceed about 5 mm in diameter. The highest effective radar reflectivity computed from in situ microphysical probes on the Learjet was 41 dBZ.

The types of cloud systems are further illustrated by the examples of Learjet and DC-8 flight tracks superimposed over NEXRAD and Geostationary Operational Environmental Satellite (GOES) imagery shown in Figs. 2a and 2b. Figure 2a shows the Learjet working feeder cells associated with multicell storms over the

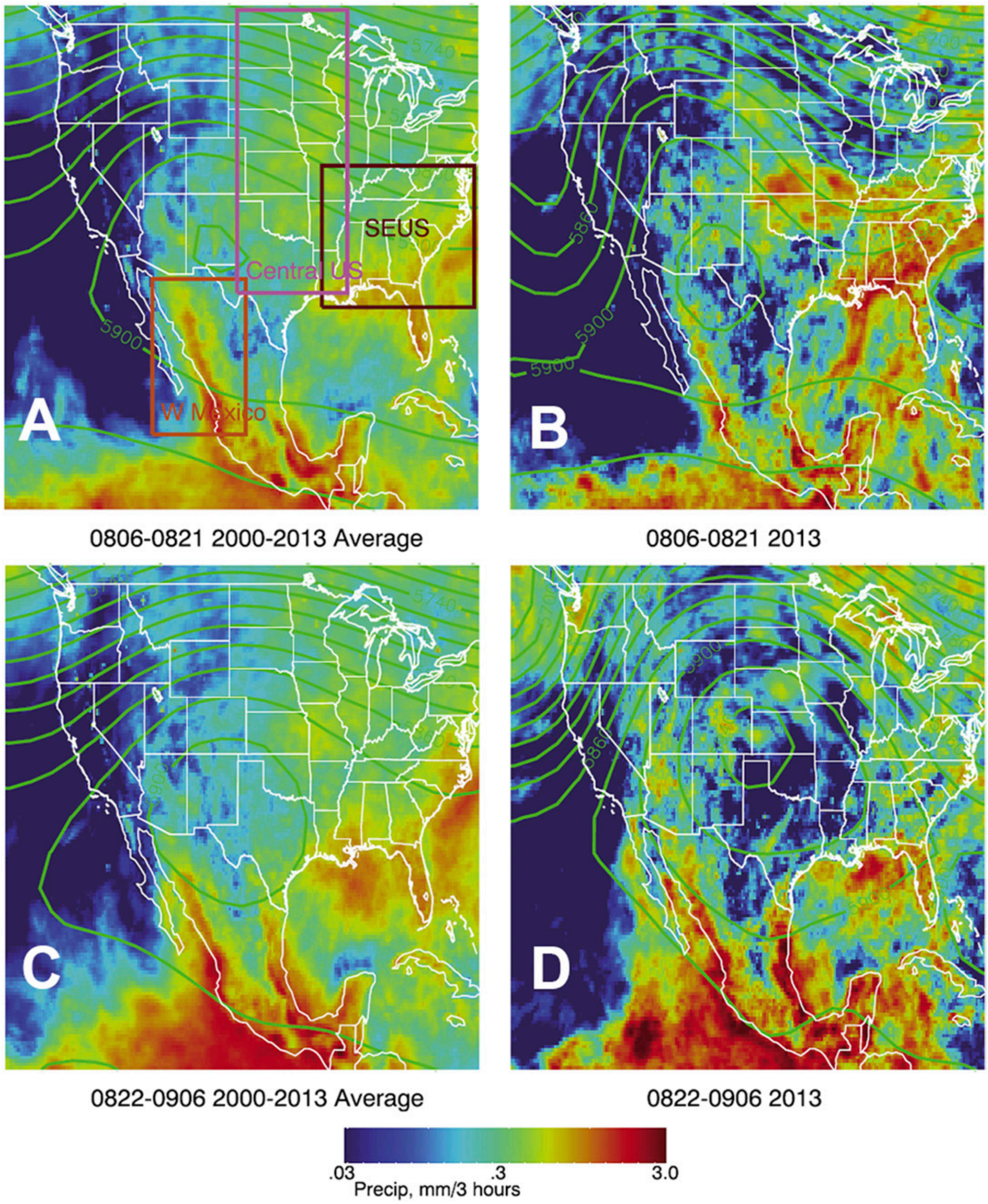

FIG. 1. Rainfall rate [mm $(3\ h)^{-1}$] (a) averaged over a 13-yr period for 6–21 Aug 2000–13 and for (b) 6–21 Aug 2013. (c) As in (a), but for the period from 22 Aug through 6 Sep 2000–13, and (d) as in (b), but from 22 Aug through 6 Sep 2013. Averaged 500-hPa heights are overplotted. Figure adapted from Toon et al. (2016), where more detail can be obtained.

Gulf. Figure 2b shows Learjet (black) and DC-8 (red) flight tracks working a coordinated study of cumulus congestus near Jackson, Mississippi. Figures 2c–e show Learjet flight tracks in Colorado and Wyoming, during SEAC^{4}RS and during Ice in Clouds Experiment–Tropical (ICE-T), respectively, where cumulus congestus and feeder cells were also investigated.

3. Measurements

a. Instrumentation

The majority of the measurements presented here were collected by the SPEC Learjet, which is described in L15 and Toon et al. (2016). Measurements near St. Croix, U.S. Virgin Islands, were acquired during the National

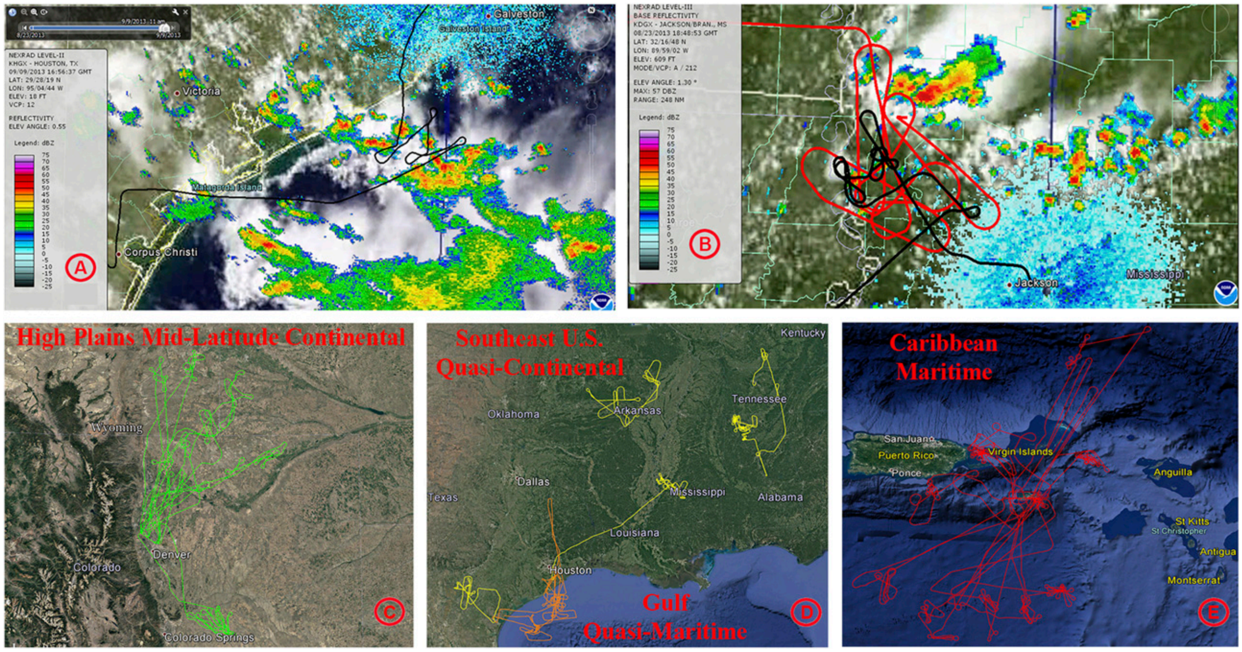

FIG. 2. Examples of NEXRAD and GOES visible satellite imagery with (a) overlay of Learjet flight track (black trace) over Gulf of Mexico; (b) Learjet flight track and NASA DC-8 flight track (red trace); (c) Learjet flight tracks in Colorado and Wyoming (green traces); (d) Learjet flight tracks during SEAC^{4}RS over Gulf of Mexico (orange traces) and the southeastern United States (yellow traces); and (e) Learjet flight tracks during ICE-T (red traces).

Science Foundation (NSF) ICE-T field project. Measurements over the Gulf of Mexico and SEUS were taken during the NASA SEAC^{4}RS project (Toon et al. 2016). Midlatitude convective cloud data over the high plains were collected by the Learjet via independent research and through partial support from the U.S. Office of Naval Research. Supporting measurements of cloud-base properties from ICE-T are contributed by a C-130 owned by the NSF and operated by the National Center for Atmospheric Research (NCAR). Cloud and aerosol measurements from a DC-8 operated by NASA during SEAC^{4}RS are also used in this analysis. A total of 57 science missions were flown by the NASA DC-8, ER-2, and SPEC Learjet during SEAC^{4}RS; the Learjet participated in 15 of the science missions. SEAC^{4}RS addressed multiple scientific objectives [see Toon et al. (2016) for a detailed description], and the Learjet was assigned various tasks, which ranged in scope from sampling growing convective updrafts in cumulus congestus to documenting the microphysical properties of outflow (anvils) from deep convection. As a result, the in situ microphysical datasets compiled in updraft cores during SEAC^{4}RS and over the high plains are not as comprehensive as obtained in ICE-T, where the scope of Learjet tasks was focused on investigations of updraft cores.

The NASA DC-8 carried 23 in situ and 5 remote sensing instruments for SEAC^{4}RS that included measurements of microphysics, aerosols, and air chemistry, along with state parameters, air motion, and position measurements. More detail on the DC-8 and Learjet instrumentation deployed during SEAC^{4}RS is available in Toon et al. (2016). Microphysical instruments on the DC-8 germane to this research were collected using a CPI (Lawson et al. 2001), a two-dimensional stereo (2D-S) optical array probe (Lawson et al. 2006), a version-3 high volume precipitation spectrometer (HVPS-3) (Lawson et al. 1998), and a fast cloud droplet probe (FCDP). These same microphysical instruments were installed on the Learjet, and, in addition, a fast forward scattering spectrometer probe (FFSSP) measured cloud DSD, and an Aventech model aircraft integrated meteorological measurement system (AIMMS-20) measured air motions. The DC-8 also carried large suites of chemistry and aerosol instrumentation. The aerosol instruments most relevant to this work are a cloud condensation nucleus (CCN) counter (Roberts and Nenes 2005) and an ultrahigh sensitivity aerosol spectrometer (UHSAS) (Cai et al. 2008), both manufactured by Droplet Measurement Technologies (DMT).

The NSF/NCAR C-130 that participated in ICE-T was equipped with an extensive payload of in situ microphysical and aerosol sensors, W-band cloud radar, and polarized lidar air motion and position measurements. More details describing C-130 instrumentation and ICE-T research missions are found in Heymsfield and Willis (2014) and L15. Data used in this paper from the NSF/NCAR C-130 were limited to DSD from an FSSP, air motion, and state parameters, described in L15. CCN measurements from the C-130 during ICE-T from Hudson and Noble (2014) are included in discussion of cloud-base aerosol properties in this paper.

b. Measurements of cloud-base temperature, drop size distributions, and aerosols

Cloud-base temperature was measured in all three field projects by climbing through cloud base or flying outside cloud at the level of cloud base. Onboard forward video was reviewed to verify notes taken by observers onboard the aircraft. Cloud-base temperature measurements include some uncertainty, since the temperature immediately below cloud base can vary depending on whether measurements are in upward- or downward-moving air, and visually estimating the level of cloud base and noting the ambient temperature can be in error because of spatial inhomogeneities. We estimate <1°C uncertainty in cloud-base temperature using these techniques. Note, however, that a 1°C error in the cloud-base temperature estimate will result in a difference of about 0.25 g m^{-3} in liquid water content (LWC) at 200 m above cloud base. The DSD within a few hundreds of meters above cloud base is an important component of the research presented in this paper. SEAC^{4}RS cloud-base DSDs were measured within about 200 m above cloud base, where there was a positive updraft velocity for at least 2 s (about 300-m spatial extent); however, most measurements were much longer than 2 s (Table 1). Clear air and air in downdrafts are not included.

Table 1 shows measurements for cloud base and other cloud penetrations discussed in this paper. Penetrations near cloud base were conducted by both the Learjet and DC-8, but the SEAC^{4}RS project did not collect systematic subcloud aerosol measurements and cloud-base DSDs in cumulus congestus clouds. Although extensive aerosol and chemistry data were collected near wild fires and over vegetation during SEAC^{4}RS (Toon et al. 2016), collection of cloud-base aerosol and DSD data was mostly ad hoc, largely because of other mission priorities.

Although coordinated aerosol and DSD measurements collected near cloud base were not the primary focus of SEAC^{4}RS, the data were sufficient to show a pattern between CCN concentration N_{ccn} and total drop concentration N_c that is consistent with results in the literature. Squires (1956, 1958a) was first to distinguish the difference in N_c near cloud base in continental and maritime convective clouds. Several studies have since concluded that N_c near cloud base in continental cumuli are 2–10 times greater than in maritime cumuli [for general reviews, see Squires and Twomey (1966), Pruppacher and Klett (1997), and Wang (2013)]. Squires (1958b) was first to postulate that DSDs were a result of the subcloud CCN. Twomey (1959) and Twomey and Squires (1959) confirmed this with direct measurements. Particularly relevant to this work, Squires and Twomey (1966) found that N_{ccn} over the high plains of Colorado was 3 times higher than over the Caribbean Sea.

Prior to 1970, measurements of the DSD just above cloud base were collected with impactor instruments and scattering probes that had a maximum range of about 50 μm. Before introduction of the 2D-S probe in 2004, measurements with optical array probes did not have adequate resolution and time response to measure the DSD between 50 and 150 μm (Lawson et al. 2006). DSD data collected within a few hundreds of meters above cloud base during ICE-T were based on Learjet and C-130 scattering probes combined with 2D-S measurements. The ICE-T DSDs from scattering probes and 2D-S showed consistent overlap in the 20–50-μm size range, which supports 2D-S measurements of DSDs with maximum diameters of at least 80 μm within a few hundreds of meters above cloud base (L15). Lowenstein et al. (2010) measured drops with maximum diameters of at least 100 μm from a combination of FSSP and 2D-S measurements in warm clouds over the Caribbean during the NSF Rain in Cumulus over the Ocean (RICO) project. While the DSD datasets of measurements near cloud base in SEAC^{4}RS and in the high plains flights are not as extensive as in ICE-T, there is consistency in the measurements and with historical results. Table 1 shows a compilation of microphysical measurements from Learjet and DC-8 measurements during SEAC^{4}RS, Learjet flights over the high plains, and relevant historical data collected in midlatitude convective clouds (i.e., Cooper et al. 1982; Knight and Squires 1982).

The RICO project, which investigated warm clouds over the Caribbean, did include systematic NSF/NCAR C-130 measurements of aerosols and DSDs within a few hundreds of meters above cloud base. One of the scientific objectives of RICO was to determine the relative influences of updraft velocity and subcloud CCN on cloud DSD. While CCN size distribution may play a role (Colon-Robles et al. 2006), Hudson and Mishra (2007) argue convincingly that variation in CCN and not updraft velocity was the major factor in the shape the DSD near cloud base. Therefore, it is reasonable to conclude that CCN size distribution plays the major role influencing DSD near cloud base.

Here we investigate data collected by the DMT CCN counter and UHSAS instruments installed on the DC-8 during SEAC^{4}RS. The CCN counter provides total

TABLE 1. Measurements collected by the Learjet (LRJ) and DC-8 (DC8) within about 200 m above cloud base (CB) and in updraft cores of all-liquid and rapid transition regions (defined in the text) in the SEUS, along the Gulf Coast near Houston and New Orleans, and over the Gulf 200–300 km offshore. VaV is vertical air velocity. Learjet measurements over the High Plains of Colorado and Wyoming are consolidated since there were not distinctive all-liquid and rapid transition regions. Historical measurements are also added for the High Plains. Weighted means are sums of individual measurements times duration divided by total duration. Note that 1 ft ≈ 0.305 m.

Date (Aircraft)	VaV start (UTC)	Altitude (ft)	CB altitude (ft)	Temp (°C)	CB temp (°C)	VaV mean ($m\,s^{-1}$)	VaV duration (s)	Liquid concentration (cm^{-3})	LWC ($g\,m^{-3}$)	Liquid Z (dBZ)
SEUS (quasi continental) cloud base										
30 Aug 2013 (LRJ)	1822:15	4980	4150	19	20.4	0.5	4	385	0.25	−36
21 Aug 2013 (DC8)	1544:18	2650	2600	21	21.5	0.5	4	566	0.18	−39
21 Aug 2013 (DC8)	1547:43	2780	2600	21	21.5	0.9	6	437	0.11	−43
21 Aug 2013 (DC8)	1548:19	2800	2600	21	21.5	1.4	11	728	0.18	−40
21 Aug 2013 (DC8)	1550:58	2830	2600	21	21.5	0.9	11	382	0.11	−42
2 Sep 2013 (DC8)	1709:00	4820	4810	19	19.8	1.9	30	822	0.18	−41
2 Sep 2013 (DC8)	1712:36	4820	4810	19	19.8	1.4	12	908	0.26	−38
2 Sep 2013 (DC8)	1716:51	4830	4810	19	19.8	2.1	8	638	0.18	−40
Weighted means				19.7	20.5	1.5		689	0.18	
Gulf Coast (quasi continental) cloud base										
4 Sep 2013 (LRJ)	1817:56	4000	3280	19.8	21	1.9	7	671	0.34	−34
16 Sep 2013 (DC8)	1636:18	3200	3100	23	23.5	0.4	6	830	0.26	−38
16 Sep 2013 (DC8)	1640:23	3220	3100	23	23.5	0.2	5	1178	0.42	−36
Weighted means				21.8	22.5	0.9		865	0.34	
Gulf (quasi maritime) cloud base										
18 Sep 2013 (LRJ)	1631:06	2330	2000	22.0	23.1	0.1	2	236	0.13	−38
18 Sep 2013 (DC8)	1505:07	2010	1900	23.0	24.0	0.3	5	215	0.04	−46
18 Sep 2013 (DC8)	1504:01	2110	1900	23.0	24.1	0.5	3	468	0.11	−42
18 Sep 2013 (DC8)	1505:23	2000	1900	23.0	23.9	0.2	2	208	0.03	−47
Weighted means				22.8	23.9	0.3		281	0.07	
High Plains (midlatitude continental) cloud base										
8 Aug 2014 (LRJ)	2434:57	14 080	13 340	1.6	3.0	1.1	6	529	0.26	−38
14 Aug 2014 (LRJ)	2302:25	13 920	12 800	4.1	6.0	3.3	8	562	0.47	−32
26 Jun 2015 (LRJ)	2053:38	11 400	9800	6.6	9.7	1.4	5	573	0.59	−30
Weighted means				4.0	6.0	2.1		554	0.44	

Date (Aircraft)	VaV start (UTC)	Temp (°C)	VaV mean ($m\,s^{-1}$)	VaV duration (s)	Liquid concentration (cm^{-3})	LWC ($g\,m^{-3}$)	Liquid Z (dBZ)	Ice concentration (L^{-1})	IWC ($g\,m^{-3}$)	Ice Z (dBZ)
SEUS (quasi continental) all-liquid										
2 Sep 2013 (LRJ)	1710:22	−0.8	10.1	13	793	3.6	−13	0	0.0	0
21 Aug 2013 (LRJ)	1731:59	−2.2	7.0	14	329	2.2	−12	0	0.0	0
21 Aug 2013 (LRJ)	1817:31	−7	3.9	5	140	3.3	6	0	0.0	0
21 Aug 2013 (LRJ)	1823:46	−4.9	3.4	4	130	5.0	13	0	0.0	0
21 Aug 2013 (LRJ)	1835:12	−4.8	3.5	3	150	3.5	6	0	0.0	0
12 Aug 2013 (LRJ)	1906:18	−0.6	4.8	2	126	1.0	−14	0	0.0	0
12 Aug 2013 (LRJ)	1908:55	−2.5	5.9	6	412	5.1	9	0	0.0	0
23 Aug 2013 (LRJ)	1939:17	0.8	7.2	3	247	1.5	−19	0	0.0	0
Weighted means			6.8		401	3.2		0	0.0	
SEUS (quasi continental) rapid transition										
23 Aug 2013 (LRJ)	1834:26	−10.9	4.4	4	41	0.0	−36	680	0.5	11
23 Aug 2013 (LRJ)	1842:34	−10.8	10.2	13	29	0.1	−18	269	0.7	12
23 Aug 2013 (LRJ)	1845:14	−13.7	9.1	12	31	0.8	−4	1209	0.7	11
23 Aug 2013 (LRJ)	1848:13	−19.1	12.3	19	25	0.2	−13	2256	1.5	13
23 Aug 2013 (LRJ)	1850:49	−18.5	8.3	19	27	0.1	−25	2210	1.6	13
Weighted Means			9.7		28	0.2		1576	1.2	
Gulf (quasi maritime) all liquid										
18 Sep 2013 (LRJ)	1516:33	0.3	3.3	3	185	3.6	10	0	0.0	0
18 Sep 2013 (LRJ)	1516:39	0.3	5.1	8	318	3.4	6	0	0.0	0
9 Sep 2013 (LRJ)	1706:11	−3.7	6.2	3	280	4.2	5	0	0.0	0

TABLE 1. (*Continued*)

Date (Aircraft)	VaV start (UTC)	Temp (°C)	VaV mean (m s^{-1})	VaV duration (s)	Liquid concentration (cm^{-3})	LWC (g m^{-3})	Liquid Z (dBZ)	Ice concentration (L^{-1})	IWC (g m^{-3})	Ice Z (dBZ)
9 Sep 2013 (LRJ)	1709:46	−4.6	5.0	6	554	3.1	−3	0	0.0	0
9 Sep 2013 (LRJ)	1716:45	1.3	3.8	4	207	4.4	10	0	0.0	0
9 Sep 2013 (LRJ)	1720:41	4.9	4.7	7	194	3.8	9	0	0.0	0
9 Sep 2013 (LRJ)	1720:54	4.9	5.7	4	165	3.5	9	0	0.0	0
9 Sep 2013 (LRJ)	1725:18	4.2	5.0	7	195	3.2	6	0	0.0	0
4 Sep 2013 (LRJ)	1901:51	11.5	8.6	5	273	3.0	−9	0	0.0	0
4 Sep 2013 (LRJ)	1907:23	4.7	6.0	3	122	7.9	13	0	0.0	0
Weighted means			5.3		264	3.8		0	0.0	
Gulf (quasi maritime) rapid transition										
9 Sep 2013 (LRJ)	1659:02	−10.4	4.2	4	45	0.7	−15	522	0.3	5
9 Sep 2013 (LRJ)	1659:10	−10.4	6.3	5	59	0.5	−18	772	0.5	7
9 Sep 2013 (LRJ)	1659:27	−10.4	4.8	4	34	0.3	−21	743	0.5	8
9 Sep 2013 (LRJ)	1703:44	−8.9	3.7	9	15	0.3	−17	967	0.6	41
9 Sep 2013 (LRJ)	1703:58	−8.9	3.5	2	13	0.3	−15	935	0.5	5
9 Sep 2013 (LRJ)	1704:04	−8.9	5.8	9	29	0.4	−13	702	0.5	8
9 Sep 2013 (LRJ)	1704:22	−8.9	3.7	2	117	0.5	−16	340	0.4	4
9 Sep 2013 (LRJ)	1709:46	−3.9	5.0	7	166	1.5	−7	380	0.3	7
Weighted means			4.8		58	0.6		694	0.5	
High plains (midlatitude continental) cloud passes										
14 Aug 2014 (LRJ)	2241:46	−13.0	5.9	2	353	1.9	−18	0	0.00	0
14 Aug 2014 (LRJ)	2244:01	−13.0	4.2	3	212	1.5	−18	0	0.00	0
17 Sep 2014 (LRJ)	2137:12	−22.6	4.3	3	341	0.3	−34	4	0.01	−7
17 Sep 2014 (LRJ)	2145:19	−25.4	3.4	2	377	0.4	−32	77	0.06	1
17 Sep 2014 (LRJ)	2148:33	−27.7	3.2	2	205	0.2	−33	432	0.50	12
29 Jul 2016 (LRJ)	1935:47	−35.5	1.9	3	128	0.6	−22	679	0.20	5
24 Apr 2015 (LRJ)	1947:25	−13.0	3.5	14	519	0.6	−27	0	0.00	0
24 Apr 2015 (LRJ)	1948:29	−12.0	3.6	5.0	507	0.4	−28	0	0.00	0
24 Apr 2015 (LRJ)	1949:09	−13.0	3.8	4.0	431	0.4	−28	0	0.00	0
Weighted means			3.6		406	0.6				
Historical High Plains data										
Cooper et al. (1982) [High Plains Cooperative Experiment (HIPLEX)]	Average CB temp = 4.6° ± 4.4°C; $N_c > 700\,\mathrm{cm}^{-3}$ with SE flow; $N_c < 400\,\mathrm{cm}^{-3}$ with NW flow									
Knight and Squires (1982) [National Hail Research Experiment (NHRE)]	Average $N_c = 800\,\mathrm{cm}^{-3}$ in unmixed cores; average $N_c = 600\,\mathrm{cm}^{-3}$ in mixed cores									

particle concentration over a range from about 0.25% to 0.50% supersaturation (SS). SS is percentage above water saturation. The counter steps through the SS range at a rate of about 0.02% SS s^{-1}. The UHSAS data presented here are aerosol total number concentration N_a over the size range measured, which is assumed to be an approximate surrogate for N_{ccn}. It is not expected that N_{ccn} and N_a will be roughly equal, but that N_{ccn} and N_a will be in phase. A complicating factor is that N_{ccn} varies directly with SS, which changes each second, so values of N_{ccn} must be compared with each other at the same SS value.

Figure 3 shows an example time series of CCN, UHSAS, and pressure altitude measurements for a DC-8 flight segment over south-central Mississippi on 2 September 2013. The absence of continuous CCN measurements is due to competition from other aerosol and chemistry instrumentation drawing from the inlet. The increase in N_{ccn} in each isolated measurement is due to increasing SS by about 0.02% each second. This is an example of one of the best comparisons we could find between N_{ccn} and N_a measurements. At other times there was little or no correlation between N_{ccn} and N_a measurements. Also, the UHSAS was not operating on several of the flights we examined. Table 2 shows averaged N_{ccn} measurements at SS = 0.35% over SEUS, Gulf Coast, and Gulf flights. The Gulf Coast flights are included because both N_{ccn} and cloud-base N_c showed more variance and increased in the average during flights along the

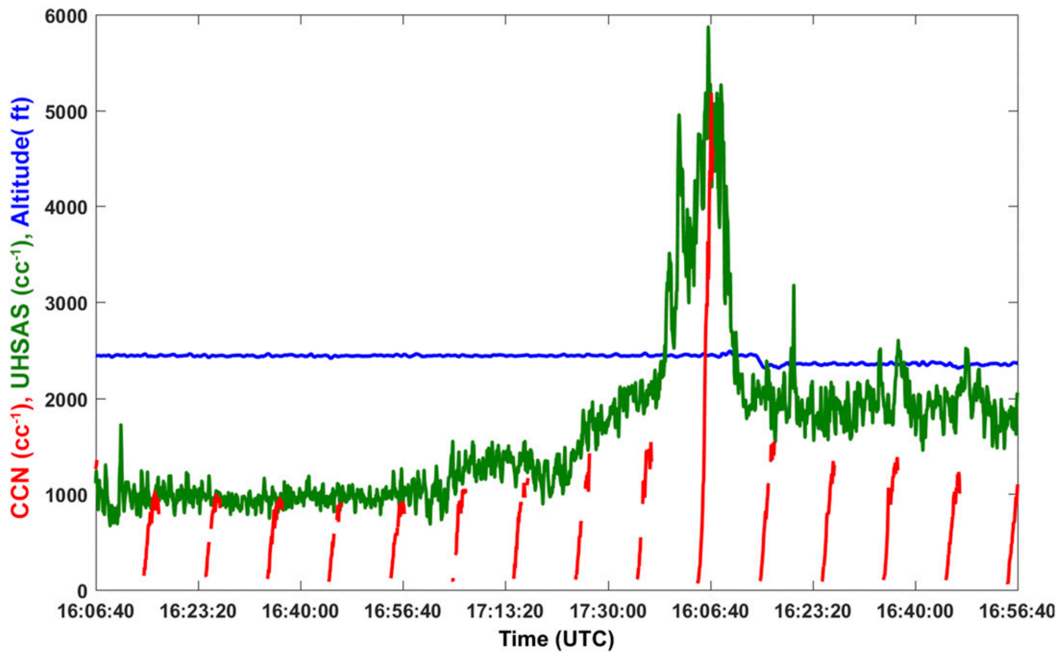

FIG. 3. Example of time series showing aircraft altitude (blue), UHSAS particle concentration (green), and CCN concentration (orange) when the DC-8 was overflying south-central Mississippi on 2 Sep 2013.

coast (Tables 1, 2). Although SEAC^{4}RS did not focus on systematic measurements of CCN and DSD near cloud base, available data (which agree with historical measurements) strongly suggest that CCN, not updraft velocity, was the driving factor impacting cloud-base DSD during SEAC^{4}RS.

3. Generation of SLDs in strong updraft cores during ICE-T and SEAC^{4}RS

Data collected in strong updraft cores between +5° and −20°C in the Caribbean are reported in detail in L15 and have provided the basis for expanding the measurements to other locations reported in this paper. Criteria used for identifying and averaging measurements in updraft cores are similar to those used in L15: To qualify, the cloud pass had to contain an updraft core that was a minimum of 2 s (~0.3 km) in duration (most are much longer; see Table 1), with a commensurate minimum vertical velocity of +3 m s^{-1}.[2] The 1-Hz measurements in downdrafts and clear air are not included. The Caribbean measurements were all collected over open ocean with no influence from continental aerosol sources.

The SEAC^{4}RS project provided an opportunity to collect data in cumulus clouds over the Gulf of Mexico, over land near highly populated urban areas on the Gulf Coast, and in the SEUS (Texas, Mississippi, Alabama, Louisiana, Arkansas, and Tennessee), as shown in Fig. 2. DC-8 CCN and DSD measurements from about 200 to 300 km from the Texas–Louisiana–Mississippi coast led us to name this region ‘‘quasi maritime.’’ This is because the DSD near cloud base is relatively broad, but N_{ccn} and N_c are higher than expected in a maritime environment (see Hudson 1993 for a review). This could be due to the proximity of urban coastal areas, heavy ship traffic, and numerous offshore oil rigs. DC-8 and Learjet measurements of DSDs near cloud base over the Gulf Coast near Houston and New Orleans, and farther inland over the SEUS are only slightly narrower than over ocean in the Gulf, but N_{ccn} and N_c are noticeably higher, so this region is called ‘‘quasi continental.’’ We describe the clouds studied in all four locations as towering cumulus cloud systems and feeder cells associated with deep convective cloud systems.

Table 1 shows average values from Learjet and DC-8 cloud penetrations analyzed in this study in the format presented for Caribbean clouds reported by L15. Values are shown for cloud-base and updraft core measurements collected by the Learjet and DC-8 over

[2] One exception is the measurement designated as 29 July 2016 (LRJ) in Table 1 with a mean updraft velocity of 1.9 m s^{-1}. This entry was included due to the unique measurement of mean LWC = 0.6 g m^{-3} at −35.5°C.

TABLE 2. CCN concentrations averaged over the time period shown and measured at SS = 0.35% by the DC-8 over the SEUS, Gulf Coast, and open ocean in the Gulf. Weighted means of concentration and standard deviation are sum of individual averages times duration divided by total duration.

Date	Region	Start (UTC)	End (UTC)	Altitude (ft)	CCN concentration (cm^{-3})	Std dev (cm^{-3})
21 Aug 2013	SEUS	1530:00	1541:40	3300	465	29
21 Aug 2013	SEUS	1543:00	1557:00	2400	203	28
2 Sep 2013	SEUS	1605:00	1655:00	2400	319	151
Weighted mean					313	105
16 Sep 2013	Gulf Coast	1626:40	1650:00	2900	501	645
18 Sep 2013	Gulf	1447:00	1501:00	430	255	53
18 Sep 2013	Gulf	1506:30	1537:00	1800	259	103
Weighted mean					258	86

the Gulf, SEUS, high plains, and for cloud-base measurements collected by the DC-8 and Learjet near Houston and New Orleans. Average cloud-base DSDs from Learjet and C-130 measurements in the Caribbean (L15) and measurements from Table 1 are shown in Fig. 4. The cloud-base temperatures in Table 1 and Fig. 4 are determined from values recorded in clear air at cloud-base elevation. The drop concentrations are averages of all aircraft penetrations within about 200 m above cloud base[3] of young turrets with "cauliflower" tops that have firm, flat cloud bases, a technique used by glider pilots to identify subcloud updrafts in developing cumulus clouds [Federal Aviation Administration (FAA 2013)]. DSDs are determined from a combination of FFSSP or FCDP and 2D-S measurements.

Based on 31 cloud penetrations, L15 report the mean ICE-T cloud-base updraft velocity at 1 $m s^{-1}$ over open ocean in the Caribbean. Table 1 shows that the mean cloud-base updraft velocities measured during SEAC^{4}RS were very similar to the average measured in ICE-T: 1.5 $m s^{-1}$ over the SEUS, 0.9 $m s^{-1}$over land on the Gulf Coast, and 0.3 $m s^{-1}$ over water in the Gulf. The mean updraft velocity was only slightly higher (2.1 $m s^{-1}$) over land in the midlatitude high plains, where the measurements were made slightly higher in the clouds and velocities are expected to be higher (Table 1).

Hudson and Noble (2014) conducted a careful aircraft study of the correlation between subcloud CCN and the DSD just above cloud base. They examined ICE-T updraft regions of subcloud CCN with uniform concentration and found a strong correlation between N_{ccn} and N_c within a few hundred meters above cloud base. Based on analysis of data from 14 ICE-T flights, they found a mean CCN concentration of 85 ± 58 cm^{-3} at a supersaturation of 0.1%, which is commensurate with the mean cloud-base DSD of 89 cm^{-3} reported by L15. They measured an average value of N_{ccn} = 151 ± 85 cm^{-3} at SS = 0.3%, which is lower, but within the standard deviation limits of the average value of 258 ± 86 cm^{-3} shown in Table 2 for Gulf measurements. Politovich and Cooper (1988) investigated 147 cumulus congestus and feeder-cell clouds that had updraft velocities similar to SEAC^{4}RS clouds and determined that SS ranged from about 0.1% to 0.4%, which is within the SS range measured by the CCN counter on the DC-8. Thus, N_{ccn} and SS measurements from the literature are commensurate with measurements from SEAC^{4}RS.

Table 2 shows CCN concentration N_{ccn} measurements collected by the DC-8 over the SEUS, Gulf Coast, and over the Gulf. The mean values of CCN concentration from Table 2 are 313 cm^{-3} over SEUS, 501 cm^{-3} over the Coast, and 258 cm^{-3} over the Gulf. The SEUS, Gulf Coast, Gulf, and Caribbean N_{ccn} measurements have the same trend as cloud-base drop concentration N_c measurements of 689 cm^{-3} over SEUS, 865 cm^{-3} over the Coast, 281 cm^{-3} over the Gulf, and 89 cm^{-3} over the Caribbean (Table 1 and Fig. 4). The low updraft velocities at cloud base in the four geographic regions listed above (mean values of 0.3–1.5 $m s^{-1}$ in Table 1), and the agreement in trend between N_{ccn} and N_c, suggest that differences in the CCN population had a more significant impact on N_c and DSD at cloud base than updraft velocity.

Squires (1958b) came to a similar conclusion over 50 years ago when he correctly surmised that the differences in microphysics were caused by similar systematic differences in the concentrations of CCN. The maritime average N_{ccn} and N_c concentrations are distinctly lower than those in the other locations. These results are in good agreement with Lowenstein et al. (2010), who used FSSP and 2D-S measurements above cloud base from the NCAR C-130 during the RICO project in the Caribbean. Lowenstein et al. (2010) measured drops with diameters of at least 100 μm in a concentration of 81 cm^{-3}, which is in good agreement with the mean ICE-T value N_c = 89 cm^{-3}.

[3] As shown in Table 1, the midlatitude clouds were penetrated slightly higher than 200 m above cloud base.

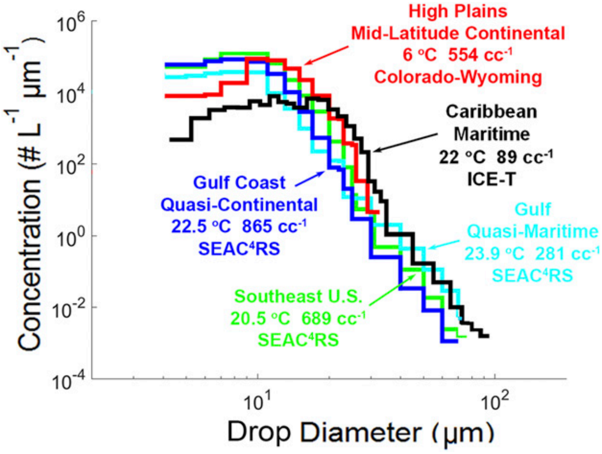

FIG. 4. Average DSDs, total drop concentration, and average cloud-base temperature measured within 200 m above cloud base at the four geographic locations described in the text.

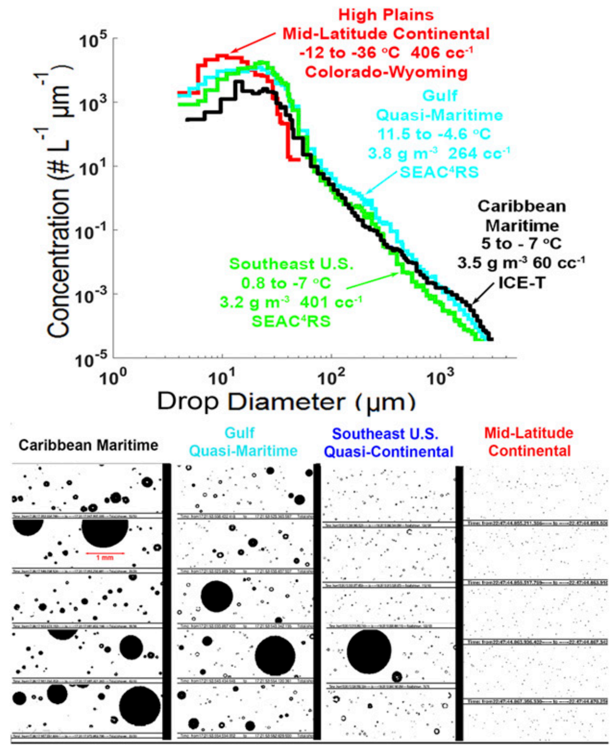

FIG. 5. Learjet observations of (top) average drop size distributions, drop concentration, and LWC measured in liquid portions of updraft cores in the temperature ranges shown in the four geographic locations described in the text. DSDs are a combination of FFSSP or FCDP, 2D-S, and HVPS measurements. (bottom) Examples of typical 2D-S images.

The top panel of Fig. 5 shows a comparison of average DSDs in the liquid portions of convective updraft cores for the Caribbean, quasi-maritime (Gulf), quasi-continental (SEUS), and high plains continental updraft cores. Table 1 shows that the average velocity in updraft cores within the temperature range from +5° to −8°C was 9.5 m s^{-1} in Caribbean clouds, 5.3 m s^{-1} from 11.5° to −4.6°C in Gulf clouds, 6.8 m s^{-1} from +0.8° to −7.0°C in SEUS clouds, and 3.6 m s^{-1} from −12.0° to −35.5°C in high plains clouds. There were far more Learjet penetrations of clouds in ICE-T than in SEAC^{4}RS, so many of the cloud penetrations with weaker updraft cores were not included in the ICE-T dataset. It is interesting to note that the maximum 1-Hz updraft velocity was higher in SEAC^{4}RS (27 m s^{-1}) than in ICE-T (21 m s^{-1})

The bottom panel of Fig. 5 shows representative 2D-S images from the four geographic locations. The midlatitude DSD has broadened from about 30 μm at cloud base to only about 50 μm 1–4 km higher in the updraft,[4] which is markedly distinct from the DSDs collected in the other three geographic locations. The maritime, Gulf, and SEUS all contain supercooled drops ≥ 1 mm in diameter 1–3 km above cloud base, which increase progressively in concentration from SEUS (198 m^{-3}) to Gulf (332 m^{-3}) to maritime (1015 m^{-3}). As was the case at cloud base, the maritime DSD has a much lower concentration of small (<30 μm)-diameter drops than the other geographic areas and a total drop concentration of 60 cm^{-3}. The Gulf (quasi maritime) has a noticeably higher total drop concentration (264 cm^{-3}) compared with maritime. SEUS (401 cm^{-3}) and high plains (406 cm^{-3}) drop concentrations are higher yet and in line with values found in the literature (Table 1). We speculate that the higher drop concentration over the Gulf compared with the Caribbean is likely due to the close proximity to industrialization along the Gulf Coast and the preponderance of oil rigs and ship traffic in the Gulf. This speculation is supported by the relatively elevated CCN concentrations over the Gulf compared with the Caribbean.

The broad cloud-base DSDs seen in the maritime, Gulf, and SEUS measurements (Fig. 4) and the relatively large warm cloud depth are likely responsible for initiating coalescence higher in these clouds. Numerical simulations suggest that collection efficiencies are low (<10%) for 30-μm-diameter drops and that drops larger than 50 μm are required for coalescence to produce drizzle drops (e.g., Cooper et al. 2011). Deconvolving the relative influences of a broad drop distribution at cloud base and a large depth of warm cloud presents a challenge. The broad DSDs at cloud base in the Caribbean, Gulf, and SEUS locations are suggestive of a more maritime subcloud CCN population,

[4] Note that the three-view CPI (3V-CPI) can be set to "fish" for particles larger than a preset cut size, and, when configured this way, a very rare ~100-μm-diameter drop is sometimes observed near cloud top.

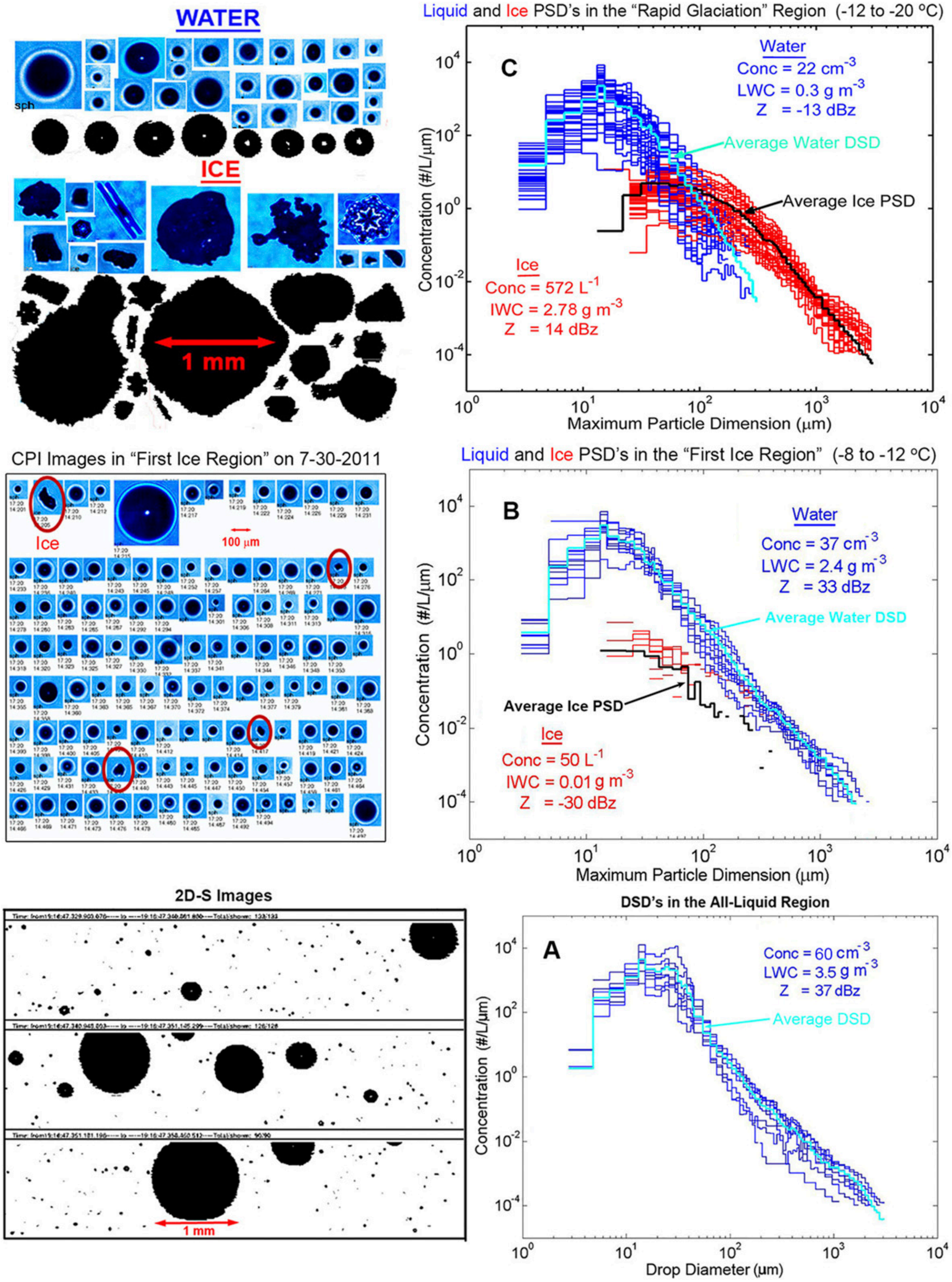

FIG. 6. Learjet measurements from ICE-T in strong updraft cores showing (bottom left) 2D-S images and (bottom right) DSDs from +5° to −7°C; (middle left) CPI images with red circles around ice particles and (middle right) PSDs separated into ice (red) and water (blue) in the region from −8° to −12°C; and (top left) 2D-S images and (top right) ice and water PSDs in the region from −12° to −20°C (adapted from L15).

which is known to be associated with the warm rain process (Hudson 1993). On the other hand, the warmer cloud base in those locations provides a larger depth of warm cloud, which also promotes increased condensational growth, drop collisions, and the coalescence process.

Figure 6 is reproduced from L15 and is shown here as a point of reference. The figure shows a composite of ice and water particle size distributions (PSDs) with particle images from Learjet penetrations of strong updraft cores during ICE-T. Liquid water content is computed assuming all water drops are spherical, and ice water content (IWC) is computed using the technique of Baker and Lawson (2006). The takeaway message from Fig. 6 is that large quantities of LWC are rapidly converted to ice in these clouds with millimeter-diameter supercooled drops. L15 determined that this rapid glaciation is not possible from primary nucleation and is also too slow and outside the temperature range of Hallett–Mossop SIP (Hallett and Mossop 1974).

The SEAC^{4}RS project incorporated multiple scientific objectives (Toon et al. 2016), and thus Learjet penetrations of fresh updraft cores were not as focused nor as abundant as in the ICE-T project. Regardless, it is still possible to analyze the data in a manner similar to that presented in L15 (e.g., Fig. 6). Figure 7 shows size distributions in the format of Fig. 6 for the all-liquid and rapid transition (from liquid to ice) regions from Gulf and SEUS penetrations of updraft cores.[5] Similar to the Caribbean, updraft cores in both the Gulf and SEUS regions experienced rapid glaciation in updraft cores prior to reaching the −20°C level. Like observations in the Caribbean (Fig. 6), the large drops in the all-liquid PSD are observed to freeze before the smaller (<~100 μm) drops.

The coldest temperature at which the Learjet observed supercooled water during ICE-T was −24°C, which was determined to be 0.005 g m^{-3} and was only detectable via CPI imagery (i.e., it was below the detection threshold of the Rosemount icing detector). An analysis of DC-8 and Learjet data from SEAC^{4}RS shows that supercooled liquid water was detectable as cold as −21°C over both the Gulf and over the SEUS. Albeit, neither of the ICE-T nor SEAC^{4}RS field campaigns were aimed at finding exactly how cold supercooled liquid exists in these convective clouds. However, recent tropical field campaigns [e.g., the NASA Kwajalein Experiment (KWAJEX); the NASA Tropical Composition, Cloud and Climate Coupling project (TC4); and the NASA African Monsoon Multidisciplinary Analyses (NAMMA) mission] have also reported a lack of supercooled liquid water at colder temperatures (Stith et al. 2004; Lawson et al. 2010; Heymsfield and Willis 2014). For example, Stith et al. (2004) reported that most updrafts observed in the KWAJEX project glaciated rapidly, removing most of the liquid water between −5° and −17°C. That said, traces of supercooled liquid can occasionally be found at much colder temperatures in tropical systems, typically in squall lines and mesoscale convective complexes, which may contain large-diameter embedded updraft cores with exceptionally strong velocities.

4. Observations of updraft cores in midlatitude continental cumulus

The 2D-S images in Fig. 5 imply that SLDs are not commonly found in midlatitude continental cumulus clouds that form over the high plains. To confirm this observation, Learjet flights were conducted in towering cumulus and feeder cells in northeast Colorado and southeast Wyoming from 2014 to 2016. An example of data from a flight on 29 July 2016 is shown in Fig. 8. From 1935:47 to 1935:55 UTC the Learjet penetrated near the top of a growing cumulus at −35.5°C. The cloud-base temperature was approximately −14°C, and the LWC during the penetration peaked at 0.7 g m^{-3}, which is 70% of the adiabatic value. Again, most of the ice particles were observed on the edges of the (5 m s^{-1} peak) updraft, but some larger (300–500 μm) particles were also mixed into the updraft core, as shown in the example images in Fig. 8. The noticeable feature of this cloud penetration is that up to 0.7 g m^{-3} of supercooled LWC was observed at −35.5°C in a mostly isolated, relatively small towering cumulus. The photograph in Fig. 8, taken after exiting the cloud, shows at least 5 mm of rime ice on unheated surfaces of the instruments and aircraft, which is a strong qualitative indicator of supercooled liquid water in the cloud. Supercooled liquid water has been observed as cold as −37.5°C in vigorous, mostly protected updrafts of feeder cells associated with large multicell storms (e.g., Rosenfeld and Woodley 2000), but there are no reports in the literature of liquid water at −35.5°C in a small towering cumulus, such as is seen in Fig. 8. A key observation here is that the large majority of LWC is found in small (<50 μm) cloud drops, which is consistent with measurements reported by Rosenfeld and Woodley (2000). In contrast, clouds that produce SLDs tend to glaciate rapidly and deplete the LWC before it can be transported to such cold levels in the updraft (Koenig 1963, 1965; L15).

It is important to reemphasize, however, that the midlatitude clouds discussed here are not associated

[5] There were too few penetrations of fresh updraft cores in the ''ice initiation'' region to provide meaningful results.

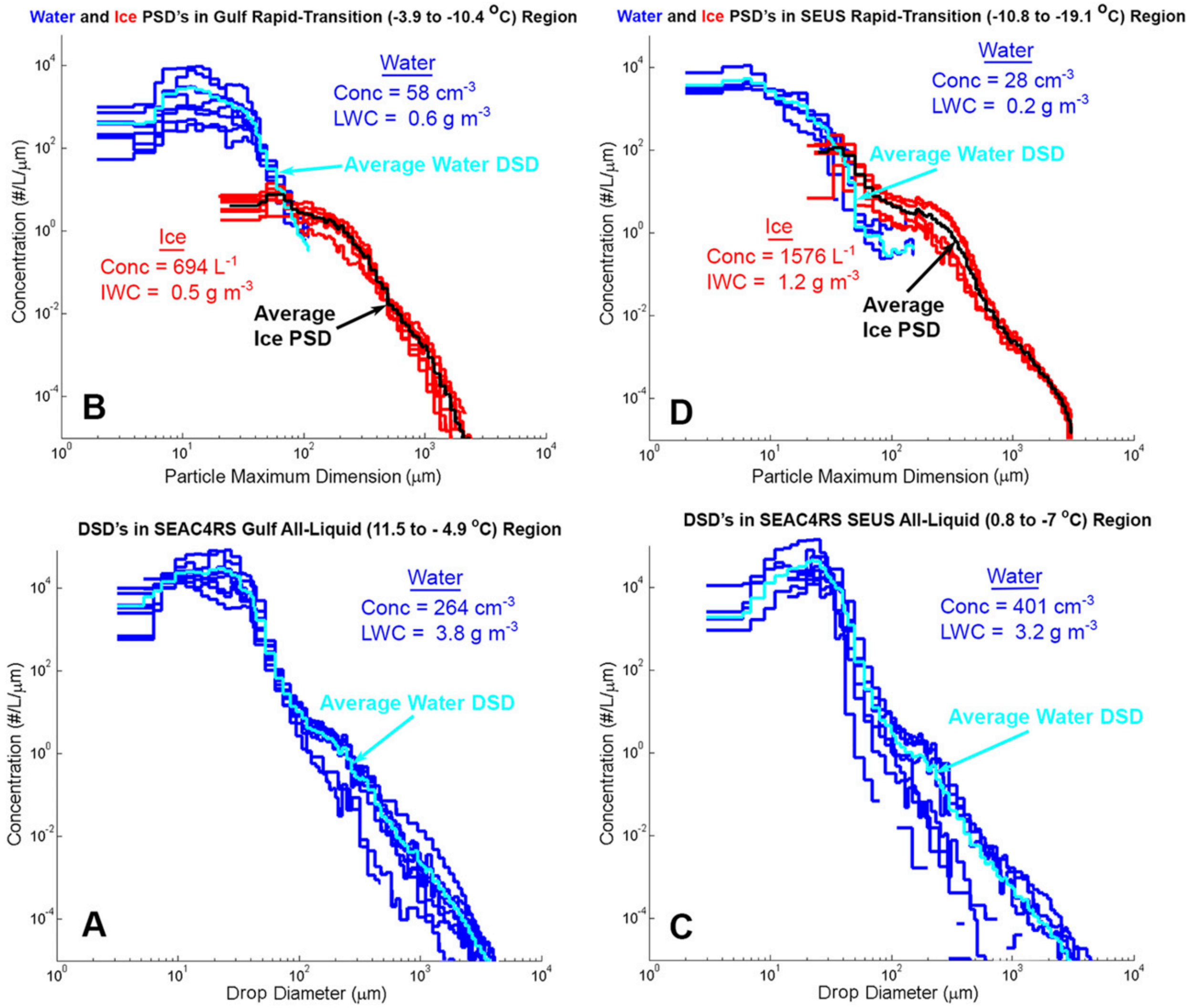

FIG. 7. Particle size distributions in the (a) all-liquid region and (b) rapid transition region of Gulf clouds and the (c) all-liquid region and (d) rapid transition region of SEUS clouds.

with supercells and other very large convective systems that spawn large-diameter (tens of kilometers) protected updrafts, which tend to transport large quantities of supercooled liquid drops from cloud base to the homogeneous freezing level, −38°C (Rosenfeld and Woodley 2000). These types of systems often have lower cloud bases than "garden variety" convective cloud systems on the high plains because of their tendency to moisten their own subcloud environment, resulting in conditions more favorable for the development of SLDs. Also, convective clouds in the Midwest (e.g., Missouri, Ohio, Kansas, Nebraska, Iowa, Illinois, and Indiana) have lower cloud bases as a result of lower surface elevations that should be more favorable to the formation of SLDs. Unfortunately, there have not been recent aircraft measurements with new instrumentation capable of confirming SLDs in strong updraft cores of Midwest systems and supercells over the High Plains.

5. SIP

The formation of SLDs is of particular interest to this research because of the rapid glaciation that is associated with their formation (Koenig 1963, 1965; L15) and the association of SLDs with a SIP based on laboratory experiments (Leisner et al. 2014; Lauber et al. 2016; Wildeman et al. 2017). Leisner et al. (2014) found that 10%–25% of 80-μm-diameter supercooled drops electrostatically suspended in the temperature range from −5° to −15°C formed spicules when freezing. As shown in Fig. 9a, the spicules form bubbles that eject tiny fragments. Leisner's work was extended by Lauber et al. (2016), who

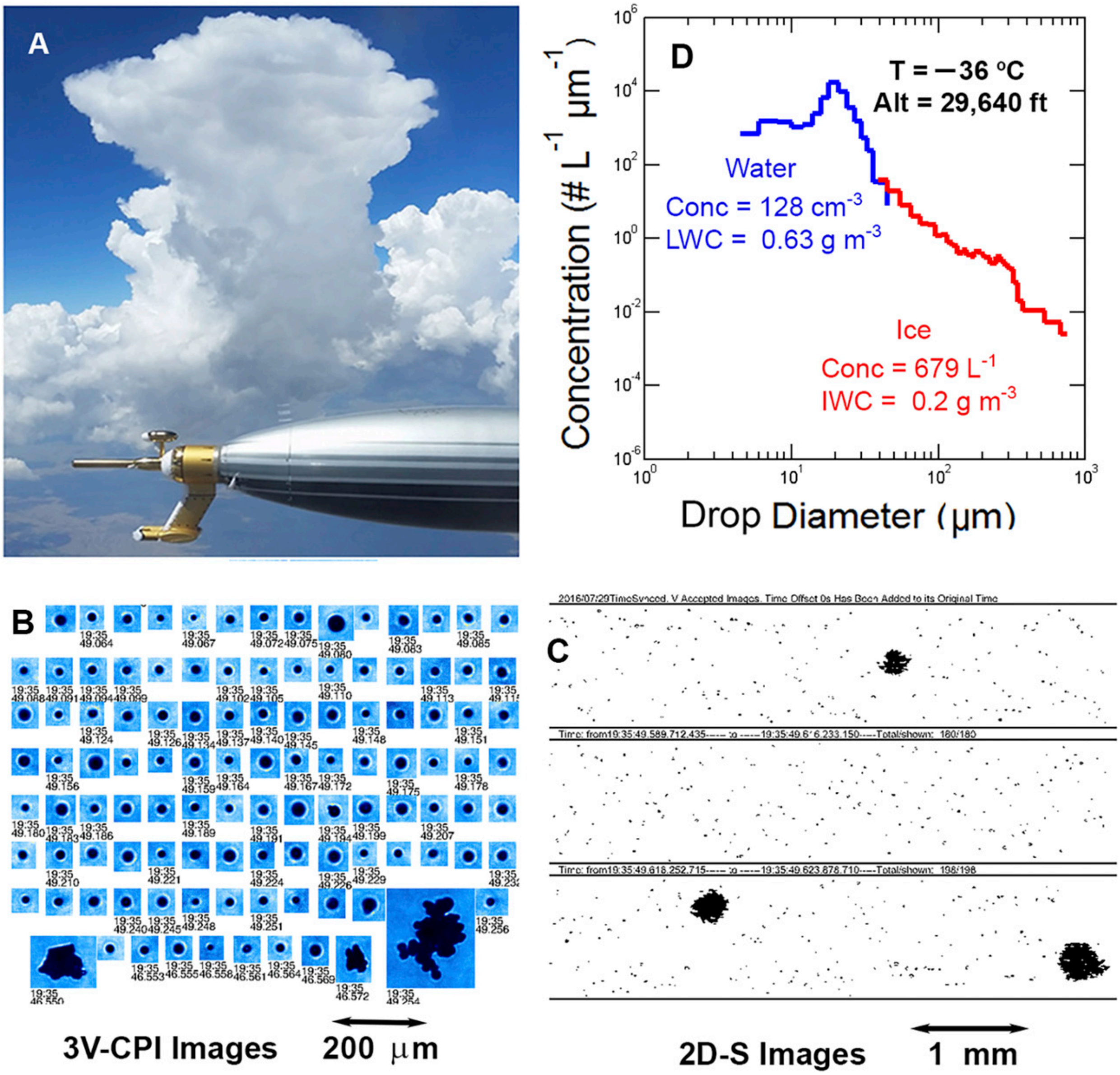

FIG. 8. (a) Photo of towering cumulus cloud about 4 min after being penetrated at −35.5°C from 1935:47 to 1935:55 UTC 29 Jul 2016. Rime ice is seen on unheated areas of tiptank instruments confirming the presence of supercooled liquid water. (b) Example of CPI images and (c) 2D-S images of supercooled water drops and ice particles collected during penetration of updraft cored at −35.5°C. (d) Particle size distributions of supercooled water drops and ice particles separated using image identification of CPI and 2D-S images collected during penetration at −35.5°C.

performed experiments on drops as large as 400 μm. The larger drops with diameters up to 400 μm either formed spicules or ejected tiny fragments without forming spicules, as shown in Fig. 9b. Lauber et al. (2016) found that, upon freezing, 40% of the 400-μm drops produced SIP, a noticeable increase over the 10%–25% frequency attributable to the 80-μm drops.

Wildeman et al. (2017) also performed high-speed videography of supercooled drops, shown in Figs. 9c–g. They observed millimeter-diameter drops supercooled to −7°C at ice saturation on a hydrophobic surface of candle soot. The drops were nucleated with AgI and shown to form spicules (Figs. 9c,d) that emitted ice fragments at 3.5 $\mathrm{m\,s^{-1}}$ (Fig. 9e), cracks on the surface where small ice was emitted, and eventually (within about 2 s), the drops exploded, ejecting several ice particles at a velocity of 1.5 $\mathrm{m\,s^{-1}}$ (Fig. 9g). The authors developed a model that showed that the elastic energy that is released internally as the drop freezes is a function of drop diameter cubed d^3, while the energy to

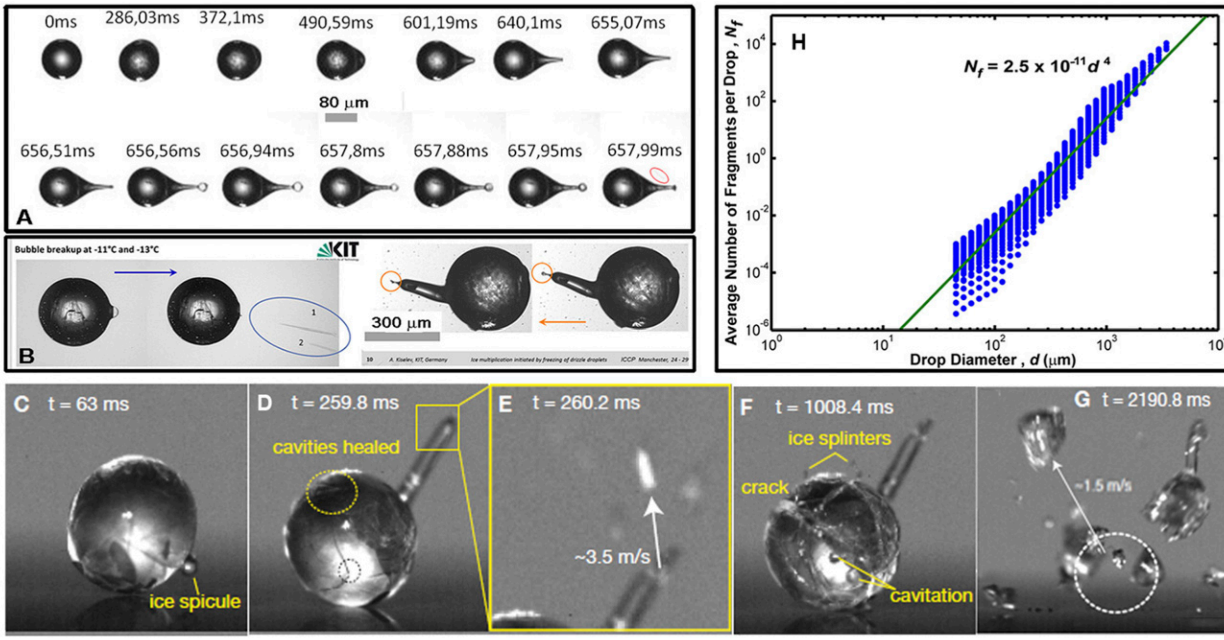

FIG. 9. (a) High-speed videography of 80-μm electrostatically suspended drop showing spicule formation and emission of particles (from Leisner et al. 2014). (b) (left) Particles being emitted from a 400-μm drop without spicule (blue ellipse with effluent tracks labeled 1 and 2) and (right) spicule formation and drop emission on 400-μm drop (from Lauber et al. 2016). High-speed videography of millimetric drops supercooled at -7 °C from Wildeman et al. (2017) showing (c),(d) spicule formation; (e) close up of ice particles emitted from the spicule at 3.5 m s^{-1}; (f) surface cracks, cavitation, and particles emitted from the surface; and (g) explosion of the drop with pieces moving at 1.5 m s^{-1} (circle is original position of the drop). (h) Plot of statistical average number of fragments per drop as a function of drop diameter extracted from model results in L15.

contain the drop via surface tension is a function of drop diameter squared d^2. The model predicts that drops with $d <\sim 100\,\mu$m will not explode. The probability of exploding increases as d^3/d^2. In their experiments, Wildeman et al. (2017) report that all millimetric drops exploded. The increase in the probability of supercooled drops to potentially emit secondary ice with increasing drop diameter agrees with the model result reported in L15, which is reproduced in Fig. 9h. The result in Fig. 9h was determined by adjusting the SIP rate in the adaptation of the Morrison and Grabowski (2010) numerical model to match the ICE-T Learjet observations.

Based on observations shown in sections 3 and 4, we find a trend that depicts the formation of SLDs as a function of cloud-base DSD and temperature. A broad DSD near cloud base is mostly reflective of the subcloud CCN population (Twomey and Squires 1959; Hudson 1993; Hudson and Mishra 2007; Hudson and Noble 2014). Regardless of the influence of CCN on DSD, it is the DSD near cloud base and the depth of warm cloud that appears to influence the formation of SLDs; that is, convective clouds with warmer bases and a broader DSD are more likely to support the coalescence process and form SLDs, whereas the drops in cold-based clouds with a narrow DSD appear to grow almost entirely through condensation. The observations show that clouds that form SLDs glaciate rapidly and at relatively warmer temperatures, whereas midlatitude convection over the high plains with much higher and colder cloud bases may transport supercooled liquid water as high as the homogeneous freezing level (~ -38°C). Given this observation, we offer the caveat that the association between SLDs and rapid glaciation in this study is empirical, and the underlying physics may (or may not) be a function of additional factors, such as drop temperature, drop composition, electrical charge, the influence of turbulence, the presence of "esoteric" ice nucleating particles, etc.

Based on the observations presented here and model results in L15, we hypothesize that the SIP described here should be a function of supercooled drop size. In other words, we argue that the SIP is strongly active in maritime convective updraft cores with high concentrations of SLDs, less active in updraft cores with smaller concentrations of SLDs, and nonexistent in clouds where the coalescence process is inactive.

The observations from ICE-T, SEAC^{4}RS, and the Learjet flights in northeast Colorado and southeast Wyoming can be used to evaluate the rate of formation of SLDs as a function of cloud-base temperature and DSD. If such a relationship were robust, the rate of production of secondary ice could be predicted using the relationship from L15 (Fig. 9h). The challenge is how to deconvolve the relationship between cloud-base temperature and DSD. Basically, we have data at the opposite ends of the chain but only limited data at the intermediate links. In simplistic terms, will a cloud with a base temperature of 22°C and a DSD that only extends out to 20 μm eventually achieve coalescence and develop SLDs and SIP? Or, alternatively, will a cloud with a 0°C cloud-base temperature and a DSD that extends out to 80 μm produce SLDs and SIP?

Unfortunately, not enough quantitative data have been collected to answer all of these questions and deconvolve the relationship between cloud-base temperature and DSD. Also, it is difficult to locate convective clouds with very cold cloud bases and broad DSDs, because convective clouds with cold bases tend to exist inland over elevated terrain and away from maritime aerosol populations or in northern climates where convection is relatively weak. It is more likely for one to find convective clouds with warm base temperatures and narrow DSDs in locations such as the low-plains states (e.g., Oklahoma, Kansas, and Iowa). Numerical models can aid in exploring these relationships, but even the most sophisticated numerical models cannot accurately predict the rate of coalescence under all conditions.

Even though we do not have sufficient measurements to deconvolve the relative influences of cloud-base temperature and DSD, it is still possible to develop an empirical relationship between these convolved parameters. The temperature $T_{\rm ice}$ (°C) at which the supercooled LWC fraction [LWC/(IWC + LWC)] decreases to less than 0.1 is computed in (1) based on average data collected from the Caribbean, Gulf, SEUS, and midlatitudes (Fig. 10):

$$T_{\rm ice} = -40e^{-0.041[(T_{\rm CB}-38)(\mathrm{DSD}_{\rm CBmax})]}, \qquad (1)$$

where $T_{\rm CB}$ (°C) is the average cloud-base temperature and $\mathrm{DSD}_{\rm CBmax}$ is the maximum drop diameter (mm) from cloud-base penetrations. Equation (1) is formulated so that $T_{\rm ice} = -40$°C when $\mathrm{DSD}_{\rm CBmax} = 0$, and $T_{\rm ice} = 0$°C when $\mathrm{DSD}_{\rm CBmax} = \infty$. The decrease in mean measured LWC in the liquid portions of strong updraft cores to about 10% in the regions where rapid glaciation occurs is arbitrary. Other values could be chosen, but the point is to select a value where rapid glaciation is mostly complete and the LWC measurement is still within the precision of the instruments. The physical basis for (1) is that strong updraft cores with warmer $T_{\rm CB}$ and larger $\mathrm{DSD}_{\rm CBmax}$ are observed to develop SLDs and glaciate more rapidly than those with colder $T_{\rm CB}$ and smaller $\mathrm{DSD}_{\rm CBmax}$. This simplistic relationship may be used as a guide to evaluate numerical simulations of the development of ice in strong updraft cores. However, more aircraft data collected in a variety of geographical regions, coupled with an improved understanding of the coalescence process is needed to deconvolve the relationship between cloud base DSD and temperature.

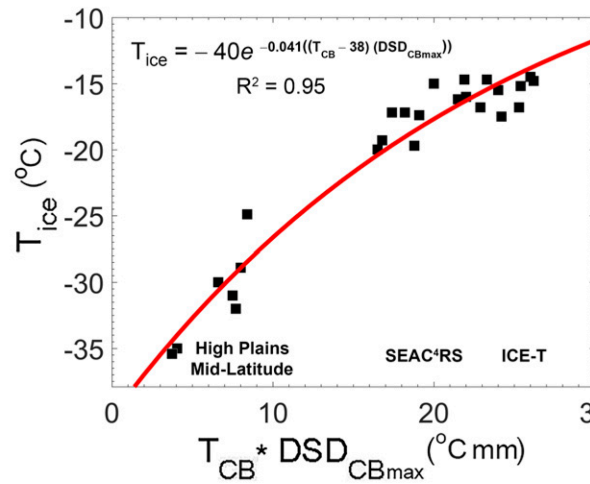

FIG. 10. Predicted value of $T_{\rm ice}$ where LWC/(LWC + IWC) < 0.1, plotted as a function of $T_{\rm CB}$ times $\mathrm{DSD}_{\rm CBmax}$. Data points are derived from aircraft measurements of average values of $T_{\rm CB}$ and $\mathrm{DSD}_{\rm CBmax}$ in the Caribbean, over the Gulf of Mexico, the southeastern United States, northeast Colorado, and southeast Wyoming. See (1) in text.

6. Summary and discussion

Microphysics and dynamics data collected by research aircraft (SPEC Learjet, NCAR/NSF C-130, and NASA DC-8) in cumulus updraft cores investigated during ICE-T (Caribbean), SEAC[4]RS (Gulf of Mexico and the southeastern United States), and Learjet flights in Colorado–Wyoming are analyzed and discussed. Cloud-base temperature and drop size distribution (DSD) measurements are correlated with observations of the DSD and ice particle size distributions as the Learjet climbs and repeatedly penetrates the updraft core. Relatively warm (19.8°–24.1°C) cloud bases with broad DSDs (out to 80 μm in diameter) in the Caribbean, Gulf, and SEUS support the development of supercooled large drops (SLDs) with diameters that exceed 1 mm (L15).

Recent laboratory experiments suggest that up to 40% of SLDs emit secondary (ice) particles when they freeze (Leisner et al. 2014; Lauber et al. 2016), and that 100% of millimeter-diameter drops explode and emit ice particles (Wildeman et al. 2017). Small ice emitted from freezing SLDs can freeze additional SLDs that have a much larger relative fall velocity. The freezing of SLDs by

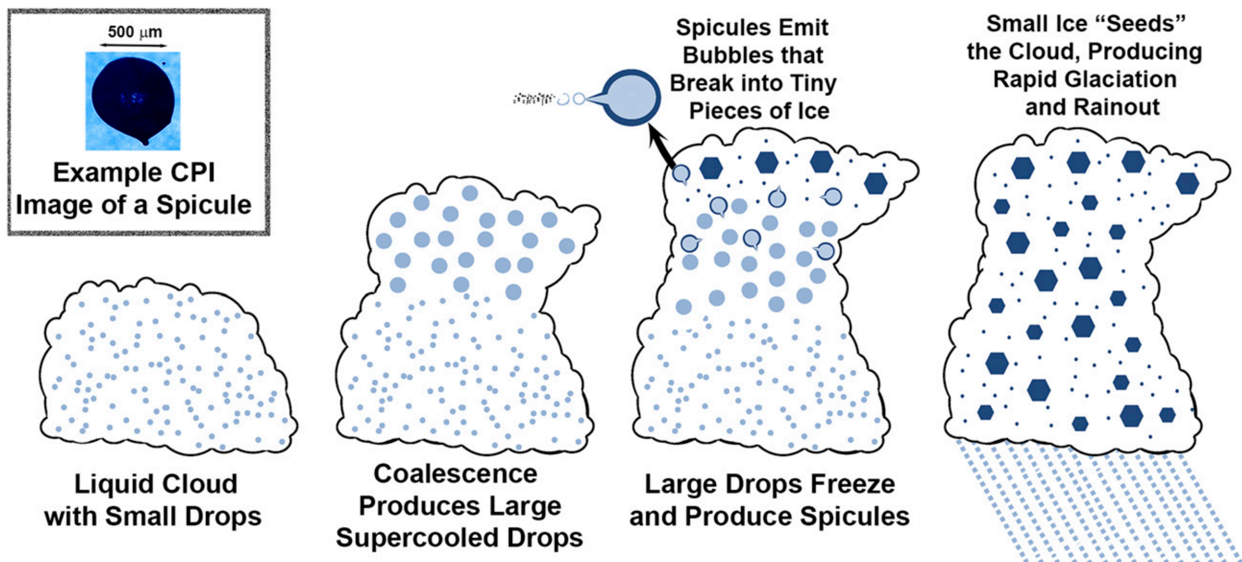

FIG. 11. Schematic diagram showing the evolution of SLDs that produce spicules, which can produce ice cannons that generate tiny ice particles. Collisions between the tiny ice and rapidly falling large supercooled drops results in rapid glaciation. (top left) CPI image of a spicule emitting a bubble that was recorded at 1748:34 UTC 18 Sep 2013 by the Learjet at −9°C.

collision with small ice particles is hypothesized to create an avalanche secondary ice process (SIP) in updraft cores, resulting in rapid glaciation. The freezing SLDs that produce spicules are like small "ice cannons," which inject small ice particles throughout the supercooled cloud region, as depicted schematically in Fig. 11.

While the avalanche SIP is not technically a new process (e.g., Koenig 1963), the mechanism and supporting laboratory evidence are new, as are the quality measurements. Aircraft observations verify that millimeter-diameter SLDs routinely develop and rapidly freeze in the updraft cores of cumulus clouds observed in both ICE-T and SEAC^{4}RS. In striking contrast, midlatitude clouds over the high plains, which have much higher and colder cloud bases and very narrow DSDs, generally do not experience coalescence, and supercooled drops rarely exceed 50 μm in diameter. Consequently, there is no obvious SIP and supercooled liquid water is transported in small drops to much colder levels in the cloud, at times reaching the homogeneous freezing level.

An empirical relationship that convolves cloud-base temperature and DSD is developed to predict the temperature in an updraft core at which the LWC fraction [LWC/(LWC + IWC)] decreases to less than about 10%. More data in various regions where convective clouds experience a larger range of environmental conditions (i.e., warm cloud bases and narrow DSDs; cold cloud bases with broad DSDs) are needed to deconvolve the relationship between cloud-base temperature and DSD. These data should also provide a better basis for evaluating the physics associated with SIP.

The rapid glaciation of clouds that form SLDs is important for our understanding of the transport of water vapor and particles into the upper troposphere and lower stratosphere (UTLS). Data from CALIOP suggest that higher mass concentrations of ice are transported into the UTLS over land compared with oceanic regions (Avery et al. 2015). The formation of SLDs and associated rapid glaciation of updrafts at warmer temperatures in maritime clouds, compared with continental clouds, may result in less mass being transported into the UTLS via deep convection over the oceans. The relationship between cloud-base temperature, DSD, and the level of glaciation developed in this paper can be used as a guide for microphysical parameterizations applied to numerical simulations of deep convection (e.g., Grabowski and Morrison 2016).

A final note is that it may be possible to trigger or stimulate the natural SIP in certain cumulus clouds that would not ordinarily develop SLDs, or develop a minimal concentration of SLDs. A mechanism to accomplish this could be via seeding at cloud base with hygroscopic material to enhance the coalescence process and stimulate the production of SLDs, resulting in rapid glaciation. The theoretical basis for enhancing the coalescence process via hygroscopic seeding is discussed in Cooper et al. (1997), and observations suggesting that hygroscopic seeding may enhance the coalescence process are presented in Mather et al. (1997) and Bruintjes (1999).

Mather et al. (1997) conducted an experiment in South Africa that bears an uncanny resemblance to the premise reported here, which is that SIP may be induced by stimulating the formation of large supercooled drops. The cloud-base temperatures of the cumulus clouds investigated were on the order of +10° to +12°C, which is in the large temperature gap between the ICE-T/SEAC^{4}RS measurements and the midlatitude continental measurements. The mean updraft velocities in the vicinity of the −10°C level were about 10 m s^{-1} and LWC was measured at 3–4 g m^{-3}, which are measurements commensurate with the ICE-T and SEAC^{4}RS.

The results from Mather et al. (1997) consistently showed that the first radar echoes in the clouds seeded at cloud base with hygroscopic material were observed near the −10°C level, and images from a 2DC probe showed millimeter drops mixed with graupel particles. Conversely, unseeded clouds did not demonstrate this consistent pattern of large drops and first radar echoes near the −10°C level. This is a striking example of an experiment that may have unexpectedly designed and documented a cloud seeding experiment that characterized the SIP we are examining here. The next step for our research plan is to sample clouds with cloud-base temperatures in a range from about +10° to +15°C to investigate the evolution of SLDs and ice and to compare results with 3D numerical models (i.e., Grabowski and Morrison 2016).

Acknowledgments. This research was funded by NASA Cooperative Agreements NNX12AC14G and NNX14AQ55G and NSF Grant AGS-1064144. Thanks to Hal Maring and Brian Toon for their cogent direction of the NASA SEAC^{4}RS project. Thanks to Alexei Korolev for helpful discussions and introducing us to the Wildeman et al. (2017) lab results.

APPENDIX

Methodologies Used to Process

a. *Cloud particle measurements and access to data repositories*

This appendix is motivated by recommendations that emerged from a ''Workshop on Data Processing, Analysis and Presentation Software'' that took place in Manchester, United Kingdom, in July 2016. The workshop, which focused on methodologies used by various groups to process data from cloud particle probes, was sanctioned by the European Fleet for Airborne Research (EUFAR) and the International Commission on Clouds and Precipitation (ICCP). Because of the myriad approaches used to process data from cloud particle probes, a recommendation was put forth that all future papers that use cloud particle measurements should include an explanation of how the data are processed and where the data can be accessed. The quantitative data presented in this paper were processed from modern forward scattering probes and optical array probes (OAPs) built by SPEC Inc. (or modified in the case of the FFSSP). This appendix discusses briefly the measurement properties of these probes, the data processing algorithms, and where the data are stored.

b. *Data repositories*

Learjet and C-130 data from the ICE-T project can be accessed online (http://data.eol.ucar.edu/master_list/?project=ICE-T). NASA SEAC^{4}RS DC-8 and Learjet data can be accessed through the NASA Langley Research Center (https://www-air.larc.nasa.gov/cgi-bin/ArcView/seac4rs?LEARJET=1). Data from the Learjet midlatitude flights are available through the SPEC ftp site and are password protected. Send an e-mail request using the form found at the SPEC website (http://www.specinc.com/contact).

c. *Scattering probe processing*

Data from three types of scattering probes, the FFSSP, the FCDP, and the Hawkeye Scattering module (Hawkeye FCDP) are presented. The operating principle for these probes is well established in the literature (e.g., Knollenberg 1981) and will not be expanded upon in this appendix. A basic summary of the relevant parameters associated with each probe is presented in Table A1.

Unlike some similar instruments, these probes record five parameters for each particle event:

TABLE A1. Summary of the scattering probes processing algorithms. For each particle sampled by the probe, the following processing criteria are applied. Acronyms are explained in the text.

	FFSSP	FCDP	Hawkeye FCDP
DOF criteria	Qual/Sig < 1.0	Qual/Sig > 0.6	Qual/Sig > 0.65
Waveform symmetry criteria	$0.6 > TT_{Full}/TT_{Peak} > 0.33$		
Transit time method	SPEC integrated Gaussian technique	SPEC integrated Gaussian technique	SPEC integrated Gaussian technique
Shattered particle filter	Arrival time algorithm	Arrival time algorithm	Arrival time algorithm

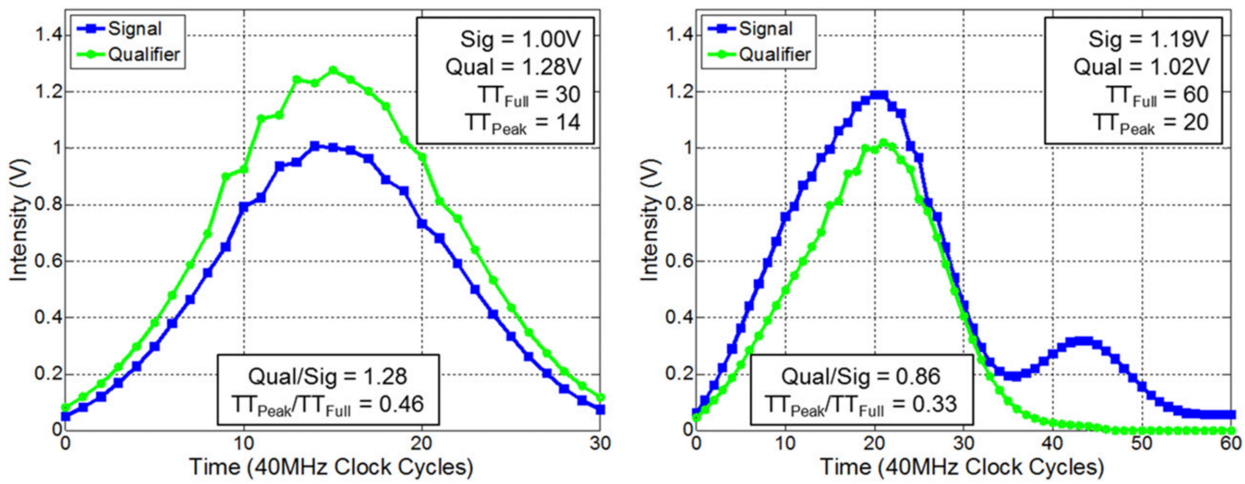

FIG. A1. Example of two raw FCDP waveforms recorded during a SPEC Learjet test flight in 2015. The waveforms from both the signal detector (blue) and qualifier detector (green) are plotted. (left) A single particle passes through the sample area of the FCDP, and a symmetric Gaussian profile is observed for both detectors. (right) A smaller particle passes through the edge of the FCDP sample area after the first particle. Because the particles are coincident in the FCDP sample area, their waveforms superimpose, which is an example of particle coincidence.

- particle start time (recorded with 0.025-μs resolution)
- signal detector peak intensity (Sig)
- qualifier detector peak intensity (Qual)
- full particle transit time (TT_{Full})
- peak particle transit time (TT_{Peak})

Data that are recorded with the particle time and other parameters are commonly called particle-by-particle data. It is also possible to record the full waveforms for a subset of particles. An example of two waveforms captured by an FCDP is presented in Fig. A1. The five parameters recorded for each particle waveform are used during postprocessing to eliminate out-of-focus particles, shattered particles, and coincident particles.

Data are processed using open-source software, which is written in Matlab and available online (www.specinc.com/downloads). Table A1 shows a summary of the scattering probe processing algorithms. The depth of field (DOF) criteria utilized for each probe is derived from laboratory calibration data and will vary for different probes. Transit time is used in conjunction with pulse height to eliminate coincident particles. The SPEC integrated Gaussian technique[A1] is used to eliminate coincident particles with relatively long transit times and low signal strengths (Fig. A1 and Table A1). The effect of shattering is minimal because of the use of antishattering probe tips and an arrival time particle removal algorithm shown in Lawson (2011).

d. OAP processing

Data for three different optical array probes, the 2D-S, HVPS-3, and Hawkeye—which houses an FCDP, CPI, and 2D-S with 10- and 50-μm channels—are discussed. The operation of these probes is described in detail elsewhere (Lawson et al. 2001, 2006; Wendisch and Brenguier 2013). During postprocessing, the individual images are analyzed for size and projected area, and algorithms are applied to remove noise, coincident

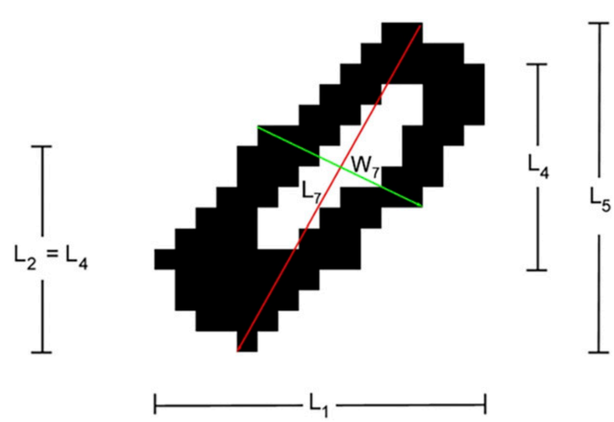

FIG. A2. Illustration showing how different length scales are defined [adapted from Lawson (2011)]. Shown are L_7 (red line) and W_7 (green line), which are new length and width scales that have not been previously defined and are used in the current processing.

[A1] The integrated Gaussian technique uses the particle transit time across the Gaussian beam profile to eliminate particles that have too long a transit time compared with signal strength. The methodology is complex and is beyond the scope of this paper. Further detail is available in the FCDP operator's manual (found at www.specinc.com/downloads).

TABLE A2. Basic components of the M_2, M_4, and M_7 image processing methods. See Fig. A2 for definitions of L_5 and L_7. SV is sample volume, TAS is true airspeed, $\Delta t_{\text{Inter-Arrival}}$ is the time differential between particles, and W_{Array} is the array width.

	M_2	M_4	M_7
All-in method	Yes	Yes	Yes
Length scale for sizing	L_5	L_5	L_7
Out-of-focus particle correction (Korolev 2007)	No	Yes	No
Sample volume	$\mathrm{SV} = \sum \mathrm{TAS} \times \Delta t_{\text{Inter-Arrival}} \times W_{\text{Array}} \times \mathrm{DOF}$		

particles, and shattered particles. The details of this process are explained in Lawson (2011), as are the various techniques used to measure the "length" of an image. The SPEC open-source software has recently been refined to incorporate two additional particle length scales not defined in Lawson (2011), which are a maximum particle length L_7 and maximum perpendicular width W_7, regardless of particle orientation, as shown in Fig. A2. A new processing method M_7, which uses L_7 and W_7, is thus added to M_2 and M_4, which are described in Lawson (2011). All three methods use the "all-in" technique (Heymsfield and Parrish 1978), which only accepts particles that do not touch the edges of the array. Method M_7 is identical in its application to M_2 with the exception that L_7 is used instead of L_5 (Fig. A2). Table A2 lists the essential methodology used in the M_2, M_4, and M_7 image processing methodologies.

The specific processing techniques used for each of the OAPs in this study are presented in Table A3. For each probe a different processing method is used for small and large particles. This distinction arises from an issue with sizing small out-of-focus particles. The particles appear as rings or "donuts" because of the presence of a Poisson spot, as seen in the small particle images in Fig. A3. The L_5 and L_7 parameters are inappropriate for these particles, so a lookup table based on the Korolev (2007) formulation is used to scale the L_5 length appropriately. Details of the out-of-focus resizing for the M_4 method can be found in appendix A of Lawson (2011).

The transition between the small and large particle size regimes is a subtle issue but can have major implications for particle area and mass distributions. An example of a particle size distribution from a series of mixed-phase cloud passes is shown in Fig. A3. The M_4 and M_7 methods produce different small particle size distributions but converge around 100 μm before diverging again. Because most small cloud particles (<~60 μm) are approximately spherical (Korolev and Isaac 2003), it is appropriate to apply the out-of-focus resizing algorithm M_4. In this example, the larger particle sizes are dominated by nonsymmetric ice, which is best characterized by the M_7 method. Therefore, in this example, a combined particle size distribution is made using the M_4 method for particles smaller than 100 μm and the M_7 method for particles larger than 100 μm. The methodologies and transition points used in processing the data analyzed in this paper are listed in the archive file headers.

TABLE A3. Summary of OAP particle classification techniques. M_4 and M_7 are defined in the text.

	2D-S	Hawkeye (10 μm)	Hawkeye (50 μm)	HVPS
Small-particle method	M_4	M_4	M_4	M_2
Large-particle method	M_7	M_7	M_7	M_7

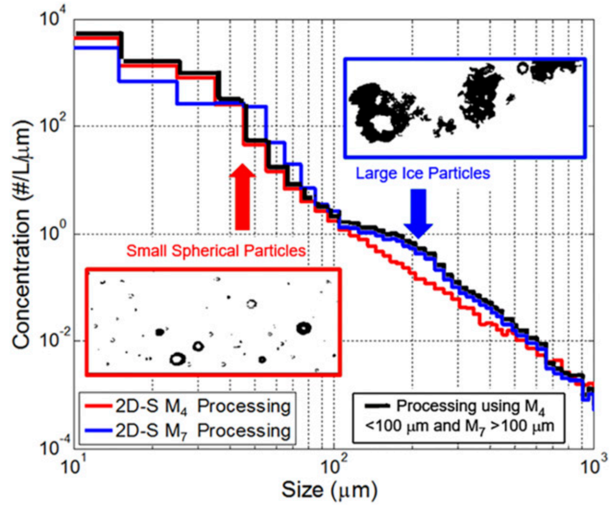

FIG. A3. A comparison of 2D-S average size distributions for a series of mixed-phase cloud passes using different postprocessing methods. The red trace is the result of processing all of the data using the M_4 method. The blue trace is the result of processing all of the data using the M_7 method. Since M_4 resizes donuts using the Korolev (2007) technique, it is not appropriate for large ice with clear areas that can be mistaken for donuts. The processing used here is a combination M_4 for particles < 100 μm and M_7 for particles > 100 μm, as shown with the black trace.

REFERENCES

Avery, M. A., and Coauthors, 2015: Marine and continental upper tropospheric convective cloud characteristics as observed during SEAC[4]RS. *Proc. SEAC[4]RS Science Team Meeting*, Pasadena, CA, California Institute of Technology. [Available online at https://espo.nasa.gov/missions/sites/default/files/documents/Tu1400_Avery_v2.pdf.]

Baker, B. A., and R. P. Lawson, 2006: Improvement in determination of ice water content from two-dimensional particle imagery. Part I: Image to mass relationships. *J. Appl. Meteor. Climatol.*, **45**, 1282–1290, doi:10.1175/JAM2398.1.

Bruintjes, R. T., 1999: A review of cloud seeding experiments to enhance precipitation and some new prospects. *Bull. Amer. Meteor. Soc.*, **80**, 805–820, doi:10.1175/1520-0477(1999)080<0805:AROCSE>2.0.CO;2.

Cai, Y., D. Montague, W. Mooiweer-Bryan, and T. Deshler, 2008: Performance characteristics of the ultra high sensitivity aerosol spectrometer for particles between 55 and 800 nm: Laboratory and field studies. *J. Aerosol Sci.*, **39**, 759–769, doi:10.1016/j.jaerosci.2008.04.007.

Cannon, T. D., J. E. Dye, and V. Toutenhoofd, 1974: The mechanism of precipitation formation in northeastern Colorado cumulus II. Sailplane measurements. *J. Atmos. Sci.*, **31**, 2148–2151, doi:10.1175/1520-0469(1974)031<2148:TMOPFI>2.0.CO;2.

Colon-Robles, M., R. M. Rauber, and J. B. Jensen, 2006: Influence of low level wind speed on droplet spectra near cloud base in trade wind cumulus. *Geophys. Res. Lett.*, **33**, L20814, doi:10.1029/2006GL027487.

Connolly, P. J., T. W. Choularton, M. W. Gallagher, K. N. Bower, M. J. Flynn, and J. A. Whiteway, 2006: Cloud-resolving simulations of intense tropical hector thunderstorms: Implications for aerosol–cloud interactions. *Quart. J. Roy. Meteor. Soc.*, **132**, 3079–3106, doi:10.1256/qj.05.86.

Cooper, W. A., R. P. Lawson, A. Rodi, and T. Cerni, 1982: Cloud physics investigations, University of Wyoming, 1977–1981. University of Wyoming Tech. Rep. 142, 129 pp.

——, R. T. Bruintjes, and G. K. Mather, 1997: Calculations pertaining to hygroscopic seeding with flares. *J. Appl. Meteor.*, **36**, 1449–1469, doi:10.1175/1520-0450(1997)036<1449:CPTHSW>2.0.CO;2.

——, S. G. Lasher-Trapp, and A. M. Blyth, 2011: Initiation of coalescence in a cumulus cloud: A beneficial influence of entrainment and mixing. *Atmos. Chem. Phys. Discuss.*, **11**, 10 557–10 613, doi:10.5194/acpd-11-10557-2011.

Dye, J. E., C. A. Knight, V. Toutenhoofd, and T. W. Cannon, 1974: The mechanism of precipitation formation in northeastern Colorado cumulus III. Coordinated microphysical and radar observations and summary. *J. Atmos. Sci.*, **31**, 2152–2159, doi:10.1175/1520-0469(1974)031<2152:TMOPFI>2.0.CO;2.

——, and Coauthors, 1986: Early electrification and precipitation development in a small, isolated Montana cumulonimbus. *J. Geophys. Res.*, **91**, 1231–1247, doi:10.1029/JD091iD01p01231.

FAA, 2013: *Glider Flying Handbook*. FAA Publ. FAA-H-8083-13A, 268 pp.

Forster, P. M. D. F., and K. P. Shine, 2002: Assessing the climate impact of trends in stratospheric water vapor. *Geophys. Res. Lett.*, **29**, 1086, doi:10.1029/2001GL013909.

Grabowski, W. W., and H. Morrison, 2016: Untangling microphysical impacts on deep convection applying a novel modeling methodology. Part II: Double-moment microphysics. *J. Atmos. Sci.*, **73**, 3749–3770, doi:10.1175/JAS-D-15-0367.1.

Hallett, J., and S. C. Mossop, 1974: Production of secondary ice particles during the riming process. *Nature*, **249**, 26–28, doi:10.1038/249026a0.

Hardiman, S. C., and Coauthors, 2015: Processes controlling tropical tropopause temperature and stratospheric water vapor in climate models. *J. Climate*, **28**, 6516–6535, doi:10.1175/JCLI-D-15-0075.1.

Heymsfield, A. J., and J. L. Parrish, 1978: A computational technique for increasing the effective sampling volume of the PMS two-dimensional particle size spectrometer. *J. Appl. Meteor.*, **17**, 1566–1572, doi:10.1175/1520-0450(1978)017<1566:ACTFIT>2.0.CO;2.

——, and P. Willis, 2014: Cloud conditions favoring secondary ice particle production in tropical maritime convection. *J. Atmos. Sci.*, **71**, 4500–4526, doi:10.1175/JAS-D-14-0093.1.

——, C. A. Knight, and J. E. Dye, 1979: Ice initiation in unmixed updraft cores in northeast Colorado cumulus congestus clouds. *J. Atmos. Sci.*, **36**, 2216–2229, doi:10.1175/1520-0469(1979)036<2216:IIIUUC>2.0.CO;2.

Hudson, J. G., 1993: Cloud condensation nuclei near marine cumulus. *J. Geophys. Res.*, **98**, 2693–2702, doi:10.1029/92JD02169.

——, and S. Mishra, 2007: Relationships between CCN and cloud microphysics variations in clean maritime air. *Geophys. Res. Lett.*, **34**, L16804, doi:10.1029/2007GL030044.

——, and S. Noble, 2014: Low-altitude summer/winter microphysics, dynamics, and CCN spectra of northeastern Caribbean small cumuli, and comparisons with stratus. *J. Geophys. Res. Atmos.*, **119**, 5445–5463, doi:10.1002/2013JD021442.

Knight, C. A., and P. Squires, 1982: *Hailstorms of the Central High Plains. I: The National Hail Research Experiment.* Colorado Associated University Press, 282 pp.

Knollenberg, R. G., 1981: Techniques for probing cloud microstructure. *Clouds: Their Formation, Optical Properties, and Effects,* P.V. Hobbs and A. Deepak, Eds., Academic Press, 15–91, doi:10.1016/B978-0-12-350720-4.50007-7.

Koenig, L. R., 1963: The glaciating behavior of small cumulonimbus clouds. *J. Atmos. Sci.*, **20**, 29–47, doi:10.1175/1520-0469(1963)020<0029:TGBOSC>2.0.CO;2.

——, 1965: Drop freezing through drop breakup. *J. Atmos. Sci.*, **22**, 448–451, doi:10.1175/1520-0469(1965)022<0448:DFTDB>2.0.CO;2.

Korolev, A. V., 2007: Reconstruction of the sizes of spherical particles from their shadow images. Part I: Theoretical considerations. *J. Atmos. Oceanic Technol.*, **24**, 376–389, doi:10.1175/JTECH1980.1.

——, and G. A. Isaac, 2003: Roundness and aspect ratio of particles in ice clouds. *J. Atmos. Sci.*, **60**, 1795–1808, doi:10.1175/1520-0469(2003)060<1795:RAAROP>2.0.CO;2.

Lauber, A., M. Schätzle, P. Handmann, A. Kiselev, and T. Leisner, 2016: Production of secondary ice particles and splintering of freezing droplets as a potential mechanism of ice multiplication. *Proc. Int. Conf. on Clouds and Precipitation*, Manchester, United Kingdom. [Available online at https://bwsyncandshare.kit.edu/dl/fiCNioFokGC4zRCLdPongUXD/ICCP_2016_Kiselev.pptx.]

Lawson, R. P., 2011: Effects of ice particles shattering on the 2D-S probe. *Atmos. Meas. Tech.*, **4**, 1361–1381, doi:10.5194/amt-4-1361-2011.

——, R. E. Stewart, and L. J. Angus, 1998: Observations and numerical simulations of the origin and development of very large snowflakes. *J. Atmos. Sci.*, **55**, 3209–3229, doi:10.1175/1520-0469(1998)055<3209:OANSOT>2.0.CO;2.

——, B. A. Baker, C. G. Schmitt, and T. L. Jensen, 2001: An overview of microphysical properties of Arctic clouds observed in May and July during FIRE ACE. *J. Geophys. Res.*, **106**, 14 989–15 014, doi:10.1029/2000JD900789.

——, D. O'Connor, P. Zmarzly, K. Weaver, B. A. Baker, Q. Mo, and H. Jonsson, 2006: The 2D-S (stereo) probe: Design and preliminary tests of a new airborne, high speed, high-resolution particle imaging probe. *J. Atmos. Oceanic Technol.*, **23**, 1462–1477, doi:10.1175/JTECH1927.1.

——, E. Jensen, D. L. Mitchell, B. Baker, Q. Mo, and B. Pilson, 2010: Microphysical and radiative properties of tropical clouds investigated in TC4 and NAMMA. *J. Geophys. Res.*, **115**, D00J08, doi:10.1029/2009JD013017.

——, S. Woods, and H. Morrison, 2015: The microphysics of ice and precipitation development in tropical cumulus clouds. *J. Atmos. Sci.*, **72**, 2429–2445, doi:10.1175/JAS-D-14-0274.1.

Leisner, T., T. Pander, P. Handmann, and A. Kiselev, 2014: Secondary ice processes upon heterogeneous freezing of cloud droplets. *14th Conf. on Cloud Physics and Atmospheric Radiation*, Boston, MA, Amer. Meteor. Soc., 2.3. [Available online at https://ams.confex.com/ams/14CLOUD14ATRAD/webprogram/Paper250221.html.]

Liu, G. S., and J. A. Curry, 1999: Tropical ice water amount and its relations to other atmospheric hydrological parameters as inferred from satellite data. *J. Appl. Meteor.*, **38**, 1182–1194, doi:10.1175/1520-0450(1999)038<1182:TIWAAI>2.0.CO;2.

Lowenstein, J., A. Blyth, and R. P. Lawson, 2010: Early evolution of the largest-sized droplets in maritime cumulus clouds. *Quart. J. Roy. Meteor. Soc.*, **136**, 708–717, doi:10.1002/qj.597.

Mather, G. K., D. E. Terblanche, F. E. Steffens, and L. Fletcher, 1997: Results of the South African cloud-seeding experiments using hygroscopic flares. *J. Appl. Meteor.*, **36**, 1433–1447, doi:10.1175/1520-0450(1997)036<1433:ROTSAC>2.0.CO;2.

Morrison, H., and W. W. Grabowski, 2010: An improved representation of rimed snow and conversion to graupel in a multicomponent bin microphysics scheme. *J. Atmos. Sci.*, **67**, 1337–1360, doi:10.1175/2010JAS3250.1.

Politovich, M. K., and W. A. Cooper, 1988: Variability of the supersaturation in cumulus clouds. *J. Atmos. Sci.*, **45**, 1651–1664, doi:10.1175/1520-0469(1988)045<1651:VOTSIC>2.0.CO;2.

Pruppacher, H. R., and J. D. Klett, 1997: *Microphysics of Clouds and Precipitation.* Kluwer Academic Publishers, 954 pp.

Roberts, G., and A. Nenes, 2005: A continuous-flow streamwise thermal-gradient CCN chamber for atmospheric measurements. *Aerosol Sci. Technol.*, **39**, 206–221, doi:10.1080/027868290913988.

Rosenfeld, D., and W. L. Woodley, 2000: Deep convective clouds with sustained supercooled liquid water down to -37.5°C. *Nature*, **405**, 440–442, doi:10.1038/35013030.

Solomon, S., and Coauthors, 2010: Contributions of stratospheric water vapor to decadal changes in the rate of global warming. *Science*, **327**, 1219–1223, doi:10.1126/science.1182488.

Squires, P., 1956: The micro-structure of cumuli in maritime and continental air. *Tellus*, **8**, 443–444, doi:10.3402/tellusa.v8i4.9040.

——, 1958a: The microstructure and colloidal stability of warm clouds. Part I: The relation between structure and stability. *Tellus*, **10**, 256–261, doi:10.1111/j.2153-3490.1958.tb02011.x.

——, 1958b: The microstructure and colloidal stability of warm clouds. Part II: The causes of the variations in microstructure. *Tellus*, **10**, 262–271, doi:10.1111/j.2153-3490.1958.tb02012.x.

——, and S. Twomey, 1966: A comparison of cloud nucleus measurements over central North America and the Caribbean Sea. *J. Atmos. Sci.*, **23**, 401–404, doi:10.1175/1520-0469(1966)023<0401:ACOCNM>2.0.CO;2.

Stith, J. L., J. A. Haggerty, A. Heymsfield, and C. A. Grainger, 2004: Microphysical characteristics of tropical updrafts in clean conditions. *J. Appl. Meteor.*, **43**, 779–794, doi:10.1175/2104.1.

Toon, O. B., and Coauthors, 2016: Planning, implementation, and scientific goals of the Studies of Emissions and Atmospheric Composition, Clouds and Climate Coupling by Regional Surveys (SEAC^{4}RS) field mission. *J. Geophys. Res. Atmos.*, **21**, 4967–5009, doi:10.1002/2015JD024297.

Twomey, S., 1959: The influence of cloud nucleus population on the microstructure and stability of convective clouds. *Tellus*, **11**, 408–411, doi:10.3402/tellusa.v11i4.9331.

——, and P. Squires, 1959: The influence of cloud nucleus population on the microstructure and stability of convective clouds. *Tellus*, **11**, 408–411, doi:10.3402/tellusa.v11i4.9331.

Wang, P. K., 2013: *Physics and Dynamics of Clouds and Precipitation.* Cambridge University Press, 450 pp.

Wendisch, M., and J. L. Brenguier, 2013: *Airborne Measurements for Environmental Research: Methods and Instruments*. Wiley, 641 pp.

Wildeman, S., S. Sterl, C. Sun, and D. Lohse, 2017: Fast dynamics of water droplets freezing from the outside in. *Phys. Rev. Lett.*, **118**, 084101, doi:10.1103/PhysRevLett.118.084101.